RICE UNIVERSITY

Investigation of the Stabilization Parameters of the Stabilized Finite Element Formulations

by

Tracee L. Curlett, 2nd Lt, USAF

A Thesis Submitted
in Partial Fulfillment of the
Requirements for the Degree

Master of Science

Approved, Thesis Committee:

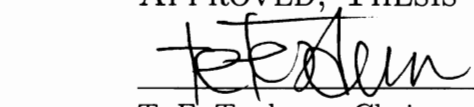

T. E. Tezduyar, Chair
Professor of Mechanical Engineering and
Materials Science

J. E. Akin
Professor of Mechanical Engineering and
Materials Science and Professor of
Computational and Applied Mathematics

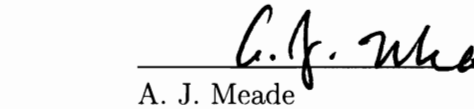

A. J. Meade
Professor of Mechanical Engineering and
Materials Science

K. Takizawa
Associate Professor in Department of
Modern Mechanical Engineering and
Waseda Institute for Advanced Study
Waseda University, Tokyo, Japan

Houston, Texas
April 2011

The views expressed in this thesis are those of the author and do not reflect the official policy or position of the United States Air Force, Department of Defense, or the U. S. Government.

Abstract

Investigation of the Stabilization Parameters of the Stabilized Finite Element Formulations

by

Tracee L. Curlett

The Team for Advanced Flow Simulation and Modeling at Rice University specializes in finite element computation of complex problems, relying on stabilized formulations such as the streamline-upwind/Petrov–Galerkin and pressure-stabilizing/Petrov–Galerkin methods. These stabilization methods involve a stabilization parameter, τ. Alternatives to the currently-used τ definitions were provided in terms of element-level matrices and vectors. An extensive investigation of these stabilization parameters is performed with comparison to currently-used τ definitions to determine their performance. Numerical data is reported to evaluate the behavior of these alternative stabilization parameters with changing element size, type, and distortion. This is accomplished through evaluation of the matrix-assembly outcome and test computations, with focus on boundary layer behavior. Test calculations are carried out in the context of a time-dependent advection–diffusion equation and the Navier–Stokes equations of incompressible flows, for both the semi-discrete formulation and the Deforming-Spatial-Domain/Stabilized Space–Time method.

Acknowledgments

First and foremost, I would like to thank my advisor, Dr. Tayfun Tezduyar. His expertise in computational modeling provided a wealth of insight and knowledge over the last two years. I would also like to offer a great deal of thanks to the members of my thesis comittee: Dr. Tezduyar, Dr. Akin, Dr. Meade, and Dr. Takizawa. I would especially like to thank Dr. Kenji Takizawa for his constant dedication to our team and research, as well as his unparalleled knowledge in computer modeling. Thank you also to the current and former members of the T★AFSM who worked with me: Lt. Moorman, Lt. Wright, Lt. Henicke, Lt. Spielman, Lt. Brummer, Matthew Fritze, Nikolay Kostov, Lt. Guertin, Lt. Montes, Lt. Puntel, and Lt. Schjodt. I am extremely thankful for this opportunity from Rice University to study at a prestigious university with such reputable professors and for the use of their facilities. I would like to thank my family and friends, no matter how far away, for their advice and support throughout my time at Rice University. I could not ask for more dedication to my goals than I have received from my parents and I could not have been successful without their help. Lastly, I would like to thank the Air Force, more specifically the Air Force Academy, who allowed me to attend this university, and several instructors and mentors who encouraged me throughout my undergraduate studies.

Contents

List of Figures

Chapter 1

Introduction

Stabilized formulations have enabled the finite element method to become a reliable and powerful approach in flow simulation and modeling. This thesis investigates currently-used and alternative selections of stabilization parameters and local length scales for several element types, including high aspect ratio and distorted elements. The stabilization parameters are described as they apply to semi-discrete and space–time formulations. Numerical evaluations utilize quadrilateral and triangular elements to evaluate differences in stabilization parameters and terms due to element type, with specific focus on boundary layer elements.

1.1 Background

Stabilized formulations are now very commonly used in finite element computation of flow problems. A brief review of the subject was provided in [33]. As explained in [33], these formulations bring numerical stability in flow problems with high Reynolds or Mach numbers and shocks or thin boundary layers, without introducing excessive numerical dissipation. They also bring numerical stability in incompressible flow computations when using equal-order interpolation functions for velocity and pressure. Some of the earliest stabilized formulations are the Streamline-Upwind/Petrov-

Galerkin (SUPG) formulation for incompressible flows [13, 5] and the SUPG formulation for compressible flows [28, 19]. The stabilized formulations introduced in [15] for advection–diffusion equations and in [31] for advection–diffusion–reaction equations included discontinuity-capturing (DC) terms. The formulation in [31] accounted for the interaction between the DC and SUPG terms by precluding the augmentation of the SUPG effect by the DC effect when the advection and discontinuity directions coincide. The formulation in [31] also included stabilization terms, which were called the "DRD" terms, to counter the numerical instabilities seen in reaction-dominated problems. The formulations introduced in [31] were applied in [31] to computation of coupled chemical and thermal transport problems governed by three coupled advection–diffusion–reaction equations — one governing the temperature, and the other two governing the concentrations of two chemical species. These formulations were extended in [32] to computation of time-dependent versions of this class of coupled chemical and thermal transport problems. The Pressure-Stabilizing/Petrov-Galerkin (PSPG) formulation for incompressible flows [22, 29] assures numerical stability while allowing us to use equal-order interpolation functions for velocity and pressure. An earlier version of this stabilized formulation for Stokes flow was introduced in [14].

As also explained in [33], in these stabilized formulations, an embedded stabilization parameter most commonly known as "τ" plays an important role. The parameter τ involves representation of the local length scales (also known as "element length") and other parameters such as the local flow velocity and the time-step size. Various element lengths and τs were proposed starting with those in [13, 5] and [28, 19], followed by the one introduced in [31]. The τ definition introduced in [31] automatically yields lower values for higher-order elements. Later, other τ definitions that are applicable to higher-order elements were proposed in [10] in the context of advective-diffusive systems. Calculating the τs based on the element-level matrices and vectors was introduced in [30] in the context of the advection–diffusion equation and the Navier–

Stokes equations of incompressible flows. These definitions are expressed in terms of the ratios of the norms of the matrices or vectors, leading to element-matrix-based (EMB) and element-vector-based (EVB) τ definitions. They automatically take into account the local length scales, advection field and the element Reynolds number. These definitions were extended in [6, 7, 8] to compressible flows. They were evaluated for higher-order elements in [1, 2] in the context of advection–diffusion equation.

The Discontinuity-Capturing Directional Dissipation (DCDD) stabilization was introduced in [23, 24] to be used with the SUPG/PSPG formulation of incompressible flows, in flow problems with sharp gradients. As mentioned in [33], the DCDD stabilization involves a second element length scale, which was also introduced in [23, 24] and is based on the solution gradient. This new element length scale is used together with the element length defined in [31]. Recognizing this second element length as a diffusion length scale, new stabilization parameters for the diffusive limit were introduced in [24, 25]. The DCDD stabilization was originally conceived in [23, 24] as an alternative to the LSIC (least-squares on incompressibility constraint) stabilization. The DCDD takes effect where there is a sharp gradient in the velocity field and introduces dissipation in the direction of that gradient. In some versions of the DCDD stabilization, the way the DCDD is added to the formulation precludes augmentation of the SUPG effect by the DCDD effect when the advection and discontinuity directions coincide. The SUPG/PSPG formulation supplemented with the DCDD stabilization was extended in [20] to turbulent flow computations. It was shown in [20] that this DCDD-suplemented formulation is very comparable in numerical performance to the SUPG/PSPG formulation supplemented with the Smagorinsky turbulence model. The "DRD" stabilization introduced in [31], and its improved versions, were applied in [9] to turbulent flow computations, and the results obtained show a good potential for this approach.

Recently the EVB τ definitions were successfully applied in [11] in the context of

the variational multiscale (VMS) method [12, 16, 17, 18, 4, 3]. The test computations reported in [11], including advection–diffusion and turbulent-flow computations, clearly showed that the EVB τ definitions are very helpful in addressing the numerical difficulties associated with using small time step sizes.

1.2 Overview

In Chapter 2 of this thesis the governing equations and stabilized formulations are presented. Chapter 3 presents the currently-used and alternative stabilization parameters for each stabilized finite element formulation.

Chapter 4 details the individual components of each stabilization parameter for a range of element shapes. Then, degeneration of quadrilateral elements is examined and degeneration of the stabilization parameter is outlined. Lastly, a study of the stabilization parameters currently used for the space–time formulation is provided. In Chapter 5, the stabilization terms are investigated for different element groupings. Two independent calculations of the stabilization terms for quadrilateral and triangle element groupings provide a detailed view of the matrices within the equation system. Modifications to the element groupings compare the effect of higher aspect ratio elements, element distortion, and nodal connectivity on assembled stabilization-term matrices. A boundary flow allows for the incorporation of the element-vector-based stabilization terms.

Chapter 6 provides computations of the stabilization parameters discussed using a semi-discrete formulation of the finite element method. Computational tests use a 2D mesh for incompressible flow past a circular cylinder exhibiting vortex shedding and compare results with past data. Next, a comparison of mesh types, with specific emphasis in the boundary layer, determines the impact of different element types on flow characteristics and stabilization parameters.

Chapter 2

Governing Equations and Stabilized Formulations

This chapter presents the governing equations and the various stabilized finite element formulations analyzed. The advection–diffusion equation and the Navier–Stokes equations of incompressible flows govern the problem for all computational results presented in this thesis. The following sections provide a summary of the stabilized formulations, with a more detailed description of the stabilization terms in Chapter 3.

2.1 Governing Equations

2.1.1 Advection–Diffusion Equation

Let us consider a domain Ω with boundary Γ the following time-dependent advection–diffusion equation, written on Ω and $\forall t \in (0, T)$ as:

$$\frac{\partial \phi}{\partial t} + \mathbf{u} \cdot \boldsymbol{\nabla} \phi - \boldsymbol{\nabla} \cdot (\nu \boldsymbol{\nabla} \phi) = 0 \text{ on } \Omega, \tag{2.1}$$

where ϕ represents the quantity being transported (e.g. temperature, concentration,

interface function), $\mathbf{u}$ is a divergence-free advection field, and ν is the diffusivity. The essential and natural boundary conditions associated with Eq. (2.1) are represented as

$$\phi = g \quad \text{on } \Gamma_g, \tag{2.2}$$

$$\mathbf{n} \cdot \nu \boldsymbol{\nabla} \phi = h \quad \text{on } \Gamma_h, \tag{2.3}$$

where g and h are given functions, $\mathbf{n}$ is the unit normal vector at the boundary, and Γ_g and Γ_h are the complementary subsets of Γ. The initial condition consists of the form

$$\phi(\mathbf{x}, 0) = \phi_0(\mathbf{x}) \text{ on } \Omega. \tag{2.4}$$

2.1.2 Navier–Stokes Equations of Incompressible Flows

Let $\Omega_t \subset \mathbb{R}^{n_{sd}}$ be the spatial fluid mechanics domain with boundary Γ_t at time $t \in (0, T)$, where the subscript t indicates the time-dependence of the spatial domain. The Navier–Stokes equations of incompressible flows can be written on Ω_t and $\forall t \in (0, T)$ as

$$\rho \left(\frac{\partial \mathbf{u}}{\partial t} + \mathbf{u} \cdot \boldsymbol{\nabla} \mathbf{u} - \mathbf{f} \right) - \boldsymbol{\nabla} \cdot \boldsymbol{\sigma} = \mathbf{0}, \tag{2.5}$$

$$\boldsymbol{\nabla} \cdot \mathbf{u} = 0, \tag{2.6}$$

where ρ, $\mathbf{u}$ and $\mathbf{f}$ are the density, velocity and the external force, respectively. The stress tensor $\boldsymbol{\sigma}$ is defined as

$$\boldsymbol{\sigma}(p, \mathbf{u}) = -p\mathbf{I} + 2\mu\boldsymbol{\varepsilon}(\mathbf{u}). \tag{2.7}$$

Here p is the pressure, $\mathbf{I}$ is the identity tensor, $\mu = \rho\nu$ is the viscosity, ν is the kinematic viscosity, and $\boldsymbol{\varepsilon}(\mathbf{u})$ is the strain-rate tensor:

$$\boldsymbol{\varepsilon}(\mathbf{u}) = \frac{1}{2}\left((\boldsymbol{\nabla}\mathbf{u}) + (\boldsymbol{\nabla}\mathbf{u})^T\right). \tag{2.8}$$

The essential and natural boundary conditions for Eq. (2.5) are represented as

$$\mathbf{u} = \mathbf{g} \text{ on } (\Gamma_t)_g, \qquad \mathbf{n}\cdot\boldsymbol{\sigma} = \mathbf{h} \text{ on } (\Gamma_t)_h, \tag{2.9}$$

where $(\Gamma_t)_g$ and $(\Gamma_t)_h$ are complementary subsets of the boundary Γ_t. A divergence-free velocity field $\mathbf{u}_0(\mathbf{x})$ is specified as the initial condition.

2.2 Stabilized Formulations

2.2.1 Advection–Diffusion Equation

Let us assume that we have constructed some suitably-defined finite-dimensional trial solution and test function spaces $\mathcal{S}_\phi^h$ and $\mathcal{V}_\phi^h$. The stabilized finite element formulation of Eq. (2.1) can then be written from [24] as follows: find $\phi^h \in \mathcal{S}_\phi^h$ such that $\forall w^h \in \mathcal{V}_\phi^h$:

$$\begin{aligned}&\int_\Omega w^h\left(\frac{\partial\phi^h}{\partial t} + \mathbf{u}^h\cdot\boldsymbol{\nabla}\phi^h\right)d\Omega + \int_\Omega \boldsymbol{\nabla}w^h\cdot\nu\boldsymbol{\nabla}\phi^h d\Omega - \int_{\Gamma_h} w^h h^h d\Gamma \\ &+\sum_{e=1}^{n_{el}}\int_{\Omega^e}\tau_{\text{SUPG}}\mathbf{u}^h\cdot\boldsymbol{\nabla}w^h\left(\frac{\partial\phi^h}{\partial t} + \mathbf{u}^h\cdot\boldsymbol{\nabla}\phi^h - \boldsymbol{\nabla}\cdot\left(\nu\boldsymbol{\nabla}\phi^h\right)\right)d\Omega = 0\end{aligned} \tag{2.10}$$

Here n_{el} is the number of elements and Ω_e is the element domain corresponding to element e, and τ_{SUPG} is the SUPG (streamline-upwind/Petrov-Galerkin) stabilization parameter to be defined with further detail in Chapter 3.

2.2.2 Navier–Stokes Equations of Incompressible Flows

Semi-Discrete Formulation

Let us again assume that we have some suitably-defined finite-dimensional trial solution and test function spaces for velocity and pressure: $\mathcal{S}_{\mathbf{u}}^h$, $\mathcal{V}_{\mathbf{u}}^h$, $\mathcal{S}_p^h$ and $\mathcal{V}_p^h = \mathcal{S}_p^h$. The stabilized finite element formulation of Eqs. (2.5)-(2.6) can then be written from [24] as follows: find $\mathbf{u}^h \in \mathcal{S}_{\mathbf{u}}^h$ and $p^h \in \mathcal{S}_p^h$ such that $\forall \mathbf{w}^h \in \mathcal{V}_{\mathbf{u}}^h$ and $\forall q^h \in \mathcal{V}_p^h$:

$$
\begin{aligned}
& \int_\Omega \mathbf{w}^h \cdot \rho \left(\frac{\partial \mathbf{u}^h}{\partial t} + \mathbf{u}^h \cdot \boldsymbol{\nabla} \mathbf{u}^h - \mathbf{f}^h \right) d\Omega + \int_\Omega \boldsymbol{\varepsilon}(\mathbf{w}^h) : \boldsymbol{\sigma}(p^h, \mathbf{u}^h) d\Omega \\
- & \int_{\Gamma_h} \mathbf{w}^h \cdot \mathbf{h}^h d\Gamma + \int_\Omega q^h \boldsymbol{\nabla} \cdot \mathbf{u}^h d\Omega \\
+ & \sum_{e=1}^{n_{el}} \int_{\Omega^e} \frac{1}{\rho} [\tau_{\text{SUPG}} \rho \mathbf{u}^h \cdot \nabla \mathbf{w}^h + \tau_{\text{PSPG}} \nabla q^h] \cdot \left[\text{Ł}(p^h, \mathbf{u}^h) - \rho \mathbf{f}^h \right] dQ \\
+ & \sum_{e=1}^{n_{el}} \int_{\Omega^e} \nu_{\text{LSIC}} \boldsymbol{\nabla} \cdot \mathbf{w}^h \rho \boldsymbol{\nabla} \cdot \mathbf{u}^h d\Omega = 0 \quad ,
\end{aligned}
\tag{2.11}
$$

where

$$
\text{Ł}(q^h, \mathbf{w}^h) = \rho \left(\frac{\partial \mathbf{w}^h}{\partial t} + \mathbf{u}^h \cdot \boldsymbol{\nabla} \mathbf{w}^h \right) - \boldsymbol{\nabla} \cdot \boldsymbol{\sigma}(q^h, \mathbf{w}^h). \tag{2.12}
$$

Here τ_{PSPG} is the PSPG (pressure-stabilizing/Petrov-Galerkin) stabilization parameter and ν_{LSIC} is the LSIC (least-squares on incompressibility constraint) stabilization parameter, both to be defined in further detail in Chapter 3.

DSD/SST Formulation

In the DSD/SST method [22, 26, 27, 24], the finite element formulation is written over a sequence of N space–time slabs Q_n, where Q_n is the slice of the space–time domain between the time levels t_n and t_{n+1}. At each time step, the integrations are performed over Q_n. The space–time finite element interpolation functions are continuous within

a space–time slab, but discontinuous from one space–time slab to another. The notation $(\cdot)_n^-$ and $(\cdot)_n^+$ will denote the function values at t_n as approached from below and above. Each Q_n is decomposed into elements Q_n^e, where $e = 1, 2, \ldots, (n_{el})_n$. The subscript n used with n_{el} is for the general case where the number of space–time elements may change from one space–time slab to another. The essential and natural boundary conditions are enforced over $(P_n)_{\mathrm{g}}$ and $(P_n)_{\mathrm{h}}$, the complementary subsets of the lateral boundary of the space–time slab. The finite element trial function spaces $(\mathcal{S}_{\mathbf{u}}^h)_n$ for velocity and $(\mathcal{S}_p^h)_n$ for pressure, and the test function spaces $(\mathcal{V}_{\mathbf{u}}^h)_n$ and $(\mathcal{V}_p^h)_n = (\mathcal{S}_p^h)_n$ are defined by using, over Q_n, first-order polynomials in space and time.

The DSD/SST formulation is written from [24] as follows: given $(\mathbf{u}^h)_n^-$, find $\mathbf{u}^h \in (\mathcal{S}_{\mathbf{u}}^h)_n$ and $p^h \in (\mathcal{S}_p^h)_n$ such that $\forall \mathbf{w}^h \in (\mathcal{V}_{\mathbf{u}}^h)_n$ and $\forall q^h \in (\mathcal{V}_p^h)_n$:

$$
\begin{aligned}
& \int_{Q_n} \mathbf{w}^h \cdot \rho \left(\frac{\partial \mathbf{u}^h}{\partial t} + \mathbf{u}^h \cdot \boldsymbol{\nabla} \mathbf{u}^h - \mathbf{f}^h \right) dQ + \int_{Q_n} \boldsymbol{\varepsilon}(\mathbf{w}^h) : \boldsymbol{\sigma}(p^h, \mathbf{u}^h) \; dQ \\
- & \int_{(P_n)_{\mathrm{h}}} \mathbf{w}^h \cdot \mathbf{h}^h \; dP + \int_{Q_n} q^h \boldsymbol{\nabla} \cdot \mathbf{u}^h \; dQ + \int_{\Omega_n} (\mathbf{w}^h)_n^+ \cdot \rho \left((\mathbf{u}^h)_n^+ - (\mathbf{u}^h)_n^- \right) d\Omega \\
+ & \sum_{e=1}^{(n_{el})_n} \int_{Q_n^e} \frac{1}{\rho} \left[\tau_{\mathrm{SUPG}} \rho \left(\frac{\partial \mathbf{w}^h}{\partial t} + \mathbf{u}^h \cdot \boldsymbol{\nabla} \mathbf{w}^h \right) + \tau_{\mathrm{PSPG}} \boldsymbol{\nabla} q^h \right] \cdot \left[\text{Ł}(p^h, \mathbf{u}^h) - \rho \mathbf{f}^h \right] dQ \\
+ & \sum_{e=1}^{(n_{el})_n} \int_{Q_n^e} \nu_{\mathrm{LSIC}} \boldsymbol{\nabla} \cdot \mathbf{w}^h \rho \boldsymbol{\nabla} \cdot \mathbf{u}^h \; dQ = 0. \qquad (2.13)
\end{aligned}
$$

This formulation is applied to all space–time slabs $Q_0, Q_1, Q_2, \ldots, Q_{N-1}$, starting with $(\mathbf{u}^h)_0^- = \mathbf{u}_0$. Here τ_{SUPG}, τ_{PSPG} and ν_{LSIC} are the SUPG, PSPG and LSIC stabilization parameters to be defined in further detail in Chapter 3.

Chapter 3

Stabilization Parameters

This Chapter details the currently-used and alternative stabilization parameters, τ used for the stabilized formulations of the semi-discrete and space–time finite element methods.

3.1 Development of the Stabilization Parameters

As pointed out in [35, 34, 26], stabilization techniques, such as the SUPG, GLS, and PSPG formulations, provide stability and accuracy to finite element problems. The SUPG formulation prevents numerical oscillations or other instabilities that might be encountered for high Reynolds number flows and strong boundary layers. The PSPG formulation allows for the use of equal-order interpolation functions without numerical instabilities for velocity and pressure. This class of stabilization parameters substantially improves convergence rate and provides superior stabilization, without introducing excessive diffusion.

One way of seeing the stabilization parameters is through a comparison of the product of the stabilization advective operator term, $(\mathbf{u} \cdot \boldsymbol{\nabla})\,\mathbf{w}$, with the time dependent and advective terms, respectively, to the Galerkin advective term. These terms yield the three commonly used definitions that combine to form the stabiliza-

tion parameter τ for the SUPG and PSPG formulations. The stabilization terms are calculated for each element.

3.2 Currently Used Stabilization Parameters

Stabilization parameters have been improved and modified over the years. This chapter presents the final form of τ, as defined in [30, 24] and updated using [35], for the flow problems investigated in this thesis.

3.2.1 Stabilized Semi-Discrete Finite Element Formulation

Defined below are the currently-used versions of the stabilization parameters for semi-discrete formulations presented in [30, 24]:

$$\tau_{\text{SUGN1}} = \left(\sum_{a=1}^{n_{en}} |\mathbf{u}^h \cdot \boldsymbol{\nabla} N_a| \right)^{-1}, \tag{3.1}$$

$$\tau_{\text{SUGN2}} = \frac{\Delta t}{2}, \tag{3.2}$$

$$\tau_{\text{SUGN3}} = \frac{h_{\text{RGN}}^2}{4\nu}, \tag{3.3}$$

where N_a is the interpolation function associated with node a and h_{RGN} is a diffusive length scale for the element (detail to follow).

Based on τ_{SUGN1}, we can define an advective length scale as follows:

$$h_{\text{UGN}} = 2\|\mathbf{u}^h\| \, \tau_{\text{SUGN1}}, \tag{3.4}$$

This definition of element length is depicted in the element-level investigation of the stabilization parameters presented in Chapter 4.

The diffusive length scale was given in [24] as follows:

$$h_{\text{RGN}} = 2 \left(\sum_{a=1}^{n_{en}} |\mathbf{r} \cdot \boldsymbol{\nabla} N_a| \right)^{-1}, \tag{3.5}$$

where $\mathbf{r}$ is calculated with the following unit vector:

$$\mathbf{r} = \frac{\boldsymbol{\nabla} \|\mathbf{u}^h\|}{\| \boldsymbol{\nabla} \|\mathbf{u}^h\| \|}. \tag{3.6}$$

An equivalent form of the unit vector $\mathbf{r}$ definition, utilized for calculations presented is:

$$\mathbf{r} = \frac{\left(\boldsymbol{\nabla} \mathbf{u}^h\right) \cdot \mathbf{u}^h}{\| \left(\boldsymbol{\nabla} \mathbf{u}^h\right) \cdot \mathbf{u}^h \|}, \tag{3.7}$$

The stabilization parameter for the SUPG and PSPG formulations is formulated from the "r-switch" [30] combination of the three components of τ.

$$(\tau_{\text{SUPG}})_{\text{UGN}} = \left(\frac{1}{\tau_{\text{SUGN1}}^r} + \frac{1}{\tau_{\text{SUGN2}}^r} + \frac{1}{\tau_{\text{SUGN3}}^r} \right)^{-\frac{1}{r}}, \tag{3.8}$$

$$(\tau_{\text{PSPG}})_{\text{UGN}} = (\tau_{\text{SUPG}})_{\text{UGN}}, \tag{3.9}$$

$$(\nu_{\text{LSIC}})_{\text{UGN}} = (\tau_{\text{SUPG}})_{\text{UGN}} \left\|\mathbf{u}^h\right\|^2. \tag{3.10}$$

Typically, $r = 2$. We note that the higher the integer r is, the sharper the switching between τ_{SUGN1}, τ_{SUGN2} and τ_{SUGN3} becomes.

All applicable remarks from [24] are included below.

Remark 1 *The "element length"s h_{UGN} (given by Eq. (3.4)) and h_{RGN} (Eq. (3.5))*

can be viewed as the local length scales corresponding to the advection- and diffusion-dominated limits, respectively.

3.2.2 DSD/SST Formulation

The space–time versions of $(\tau_{\text{SUPG}})_{\text{UGN}}$, $(\tau_{\text{PSPG}})_{\text{UGN}}$, and $(\nu_{\text{LSIC}})_{\text{UGN}}$ are defined as presented in [24]:

$$\tau_{\text{SUGN12}} = \left(\sum_{a=1}^{n_{en}} \left| \frac{\partial N_a}{\partial t} + \mathbf{u}^h \cdot \boldsymbol{\nabla} N_a \right| \right)^{-1}, \tag{3.11}$$

$$\tau_{\text{SUGN3}} = \frac{h_{\text{RGN}}^2}{4\nu}, \tag{3.12}$$

$$(\tau_{\text{SUPG}})_{\text{UGN}} = \left(\frac{1}{\tau_{\text{SUGN12}}^2} + \frac{1}{\tau_{\text{SUGN3}}^2} \right)^{-\frac{1}{2}}, \tag{3.13}$$

$$(\tau_{\text{PSPG}})_{\text{UGN}} = (\tau_{\text{SUPG}})_{\text{UGN}}, \tag{3.14}$$

$$(\nu_{\text{LSIC}})_{\text{UGN}} = (\tau_{\text{SUPG}})_{\text{UGN}} \left\| \mathbf{u}^h \right\|^2, \tag{3.15}$$

where n_{en} is the number of (space–time) element nodes and N_a is the space–time shape function associated with the space–time node a. Additionally, h_{RGN} is defined by Equation (3.5) for space-time element nodes and shape functions.

3.3 Element-Level Matrices and Vectors

Finite element computations involve calculation of element-level matrices or vectors. The decision on which approach to use depends on the trade-off between computation time and memory. For element-level vectors presented in this thesis, the time derivative of the unknown is approximated as:

$$\frac{(\mathbf{U})_{n+1} - (\mathbf{U})_n}{\triangle t} \,, \tag{3.16}$$

where $\mathbf{U}$ represents a generic unknown, $\triangle t$ is the time-step size, and n is the time level.

3.4 Alternative Stabilization Parameters

The alternative stabilization parameters presented in [30, 24] are calculated by defining stabilization parameters in terms of element-level matrices and vectors. By defining the three components of the stabilization parameter in terms of a ratio of the norms of relevant matrices or vectors, a comparable representation of each component can be found. These alternative components inherently take into account the local length scales, advection field, and element-level Reynolds number. Element-vector-based τ is solution dependent beyond the dependence on the advection field and $\mathbf{r}$.

3.4.1 Stabilized Semi-Discrete Finite Element Formulation

Advection–Diffusion Equation

From [30], let us use the notation $\mathbf{b} : \int_{\Omega_e}(\ldots)d\Omega : \mathbf{b}_\mathrm{v}$ to denote the element-level matrix $\mathbf{b}$ and element-level vector $\mathbf{b}_\mathrm{v}$ corresponding to the element-level integration

term $\int_{\Omega_e}(\ldots)d\Omega$. We now define the following element-level matrices and vectors:

$$\mathbf{m}: \quad \int_{\Omega_e} w^h \frac{\partial \phi^h}{\partial t} d\Omega \quad : \mathbf{m}_{\mathrm{V}}, \tag{3.17}$$

$$\mathbf{c}: \quad \int_{\Omega_e} w^h \mathbf{u}^h \cdot \boldsymbol{\nabla} \phi^h d\Omega \quad : \mathbf{c}_{\mathrm{V}}, \tag{3.18}$$

$$\mathbf{k}: \quad \int_{\Omega_e} \boldsymbol{\nabla} w^h \cdot \nu \boldsymbol{\nabla} \phi^h d\Omega \quad : \mathbf{k}_{\mathrm{V}}, \tag{3.19}$$

$$\tilde{\mathbf{k}}: \quad \int_{\Omega_e} \mathbf{u}^h \cdot \boldsymbol{\nabla} w^h \ \mathbf{u}^h \cdot \boldsymbol{\nabla} \phi^h d\Omega \quad : \tilde{\mathbf{k}}_{\mathrm{V}}, \tag{3.20}$$

$$\tilde{\mathbf{c}}: \quad \int_{\Omega_e} \mathbf{u}^h \cdot \boldsymbol{\nabla} w^h \frac{\partial \phi^h}{\partial t} d\Omega \quad : \tilde{\mathbf{c}}_{\mathrm{V}}. \tag{3.21}$$

The following element-level matrices and vectors $\mathbf{c}_{\mathrm{r}}$, $\tilde{\mathbf{k}_{\mathrm{r}}}$, $(\mathbf{c}_{\mathrm{r}})_{\mathrm{V}}$, and $(\tilde{\mathbf{k}_{\mathrm{r}}})_{\mathrm{V}}$ from [24] are used to define the diffusive limit of τ in a fashion compatible with Equation (3.3):

$$\mathbf{c}_{\mathrm{r}}: \quad \int_{\Omega^e} w^h \cdot \rho(\mathbf{r} \cdot \boldsymbol{\nabla} \phi^h) d\Omega \quad : (\mathbf{c}_{\mathrm{r}})_{\mathrm{V}}\ , \tag{3.22}$$

$$\tilde{\mathbf{k}_{\mathrm{r}}}: \quad \int_{\Omega^e} (\mathbf{r} \cdot \boldsymbol{\nabla} w^h) \cdot \rho(\mathbf{r} \cdot \boldsymbol{\nabla} \phi^h) d\Omega \quad : (\tilde{\mathbf{k}_{\mathrm{r}}})_{\mathrm{V}}\ . \tag{3.23}$$

We define the element-level Reynolds and Courant numbers as follows [30, 24]:

$$Re = \frac{\|\mathbf{u}^h\|^2}{\nu} \frac{\|\mathbf{c}\|}{\|\tilde{\mathbf{k}}\|}, \tag{3.24}$$

$$Cr_u = \frac{\Delta t}{2} \frac{\|\mathbf{c}\|}{\|\mathbf{m}\|}, \tag{3.25}$$

$$Cr_\nu = \frac{\Delta t}{2} \frac{\|\mathbf{k}\|}{\|\mathbf{m}\|}, \tag{3.26}$$

$$Cr_{\tilde{\nu}} = \frac{\Delta t}{2} \tau_{\mathrm{SUPG}} \frac{\|\tilde{\mathbf{k}}\|}{\|\mathbf{m}\|}, \tag{3.27}$$

where $\|\mathbf{b}\|$ is the norm of matrix $\mathbf{b}$.

As reported in [30] and updated in [24], the components of element-matrix-based

τ_{SUPG} are defined as follows:

$$\tau_{\text{S1}} = \frac{\|\mathbf{c}\|}{\|\tilde{\mathbf{k}}\|}, \tag{3.28}$$

$$\tau_{\text{S2}} = \frac{\Delta t}{2}\frac{\|\mathbf{c}\|}{\|\tilde{\mathbf{c}}\|}, \tag{3.29}$$

$$\tau_{\text{S3}} = \tau_{\text{S1}}\frac{\|\mathbf{c}\|}{\nu\,\|\tilde{\mathbf{k}}_{\text{r}}\|} \quad \text{or} \quad \tau_{\text{S1}}\,Re\left(\frac{h_{\text{RGN}}}{h_{\text{UGN}}}\right)^2. \tag{3.30}$$

All applicable remarks from [30] are included below.

Remark 2 *In the special case of a 1D problem,* $\tau_{S1} = \left(\frac{h}{2|u|}\right), \tau_{S2} = \left(\frac{\Delta t}{2}\right)$ *and* $\tau_{S3} = \left(\frac{h^2}{4\nu}\right)$*, which are the popular limits for* τ_{SUPG} *for the advection-dominated, transient-dominated and diffusion-dominated cases, respectively.*

We again use the r-switch to form

$$\tau_{\text{SUPG}} = \left(\frac{1}{\tau_{\text{S1}}^r} + \frac{1}{\tau_{\text{S2}}^r} + \frac{1}{\tau_{\text{S3}}^r}\right)^{-\frac{1}{r}}. \tag{3.31}$$

Remark 3 *It is conceivable that we calculate a separate* τ *for each element node, or degree of freedom, or element equation. In that case, each component of* τ *would be calculated separately for each element node, or degree of freedom, or element equation. For this, we first represent an element matrix* $\mathbf{b}$ *in terms of its row vectors or row matrices:* $\mathbf{b}_1, \mathbf{b}_2, \ldots, \mathbf{b}_{n_{ex}}$*. If we want a separate* τ *for each element node, then* $\mathbf{b}_1, \mathbf{b}_2, \ldots, \mathbf{b}_{n_{ex}}$*, would be the row matrices corresponding to each element node, with* $n_{ex} = n_{en}$*, where* n_{en} *is the number of element nodes. If we want a separate* τ *for each degree of freedom, then* $\mathbf{b}_1, \mathbf{b}_2, \ldots, \mathbf{b}_{n_{ex}}$*, would be the row matrices corresponding to each degree of freedom, with* $n_{ex} = n_{dof}$*, where* n_{dof} *is the number of degrees of freedom. If we want a separate* τ *for each element equation, then* $\mathbf{b}_1, \mathbf{b}_2, \ldots, \mathbf{b}_{n_{ex}}$ *would be the row vectors corresponding to each element equation, with* $n_{ex} = n_{ee}$*, where* n_{ee} *is the number of element equations. Based on this, the components of* τ *would be*

calculated using the norms of these row matrices or vectors, instead of the element matrices. For example,a separate τ_{S1} for each element node would be calculated by using the expression $(\tau_{S1})_a = \frac{\|\mathbf{c}_a\|}{\|\tilde{\mathbf{k}}_a\|}$, $a = 1, 2, \ldots, n_{en}$. We should also note that in some special cases some of these alternative ways of computing τ might give the same result.

The components of the element-vector-based τ_{SUPG} are defined as follows [30, 24]:

$$\tau_{\text{SV1}} = \frac{\|\mathbf{c}_{\text{V}}\|}{\|\tilde{\mathbf{k}}_{\text{V}}\|}, \tag{3.32}$$

$$\tau_{\text{SV2}} = \frac{\|\mathbf{c}_{\text{V}}\|}{\|\tilde{\mathbf{c}}_{\text{V}}\|}, \tag{3.33}$$

$$\tau_{\text{SV3}} = \tau_{\text{SV1}} \frac{\|\mathbf{c}\|}{\nu \, \|\tilde{\mathbf{k}}_{\text{r}}\|} \quad \text{or} \quad \tau_{\text{SV1}} \, Re \left(\frac{h_{\text{RGN}}}{h_{\text{UGN}}} \right)^2 . \tag{3.34}$$

With these three components,

$$(\tau_{\text{SUPG}})_{\text{V}} = \left(\frac{1}{\tau_{\text{SV1}}^r} + \frac{1}{\tau_{\text{SV2}}^r} + \frac{1}{\tau_{\text{SV3}}^r} \right)^{-\frac{1}{r}} . \tag{3.35}$$

All applicable remarks from [30] are included below.

Remark 4 *The definition of τ_{SUPG} given by Eq. (3.35) can be seen as a nonlinear definition because it depends on the solution. However, in marching from time level n to $n+1$ the element vectors can be evaluated at level n. This might be preferable in some cases.*

Navier–Stokes Equations for Incompressible Flows

We now define the following element-level matrices and vectors according to [30]:

$$\mathbf{m}: \quad \int_{\Omega_e} \mathbf{w}^h \cdot \rho \frac{\partial \mathbf{u}^h}{\partial t} d\Omega \quad : \mathbf{m}_{\mathrm{v}}, \tag{3.36}$$

$$\mathbf{c}: \quad \int_{\Omega_e} \mathbf{w}^h \cdot \rho(\mathbf{u}^h \cdot \boldsymbol{\nabla}\mathbf{u}^h) d\Omega \quad : \mathbf{c}_{\mathrm{v}}, \tag{3.37}$$

$$\mathbf{k}: \quad \int_{\Omega_e} \boldsymbol{\varepsilon}(\mathbf{w}^h) : 2\mu\boldsymbol{\varepsilon}(\mathbf{u}^h) d\Omega \quad : \mathbf{k}_{\mathrm{v}}, \tag{3.38}$$

$$\mathbf{g}: \quad \int_{\Omega_e} (\boldsymbol{\nabla} \cdot \mathbf{w}^h) p^h d\Omega \quad : \mathbf{g}_{\mathrm{v}}, \tag{3.39}$$

$$\mathbf{g}^{\mathrm{T}}: \quad \int_{\Omega_e} q^h (\boldsymbol{\nabla} \cdot \mathbf{u}^h) d\Omega \quad : \mathbf{g}_{\mathrm{v}}^{\mathrm{T}}, \tag{3.40}$$

$$\tilde{\mathbf{k}}: \quad \int_{\Omega_e} (\mathbf{u}^h \cdot \boldsymbol{\nabla}\mathbf{w}^h) \cdot \rho(\mathbf{u}^h \cdot \boldsymbol{\nabla}\mathbf{u}^h) d\Omega \quad : \tilde{\mathbf{k}}_{\mathrm{v}}, \tag{3.41}$$

$$\tilde{\mathbf{c}}: \quad \int_{\Omega_e} (\mathbf{u}^h \cdot \boldsymbol{\nabla}\mathbf{w}^h) \cdot \rho \frac{\partial \mathbf{u}^h}{\partial t} d\Omega \quad : \tilde{\mathbf{c}}_{\mathrm{v}}, \tag{3.42}$$

$$\tilde{\gamma}: \quad \int_{\Omega_e} (\mathbf{u}^h \cdot \boldsymbol{\nabla}\mathbf{w}^h) \cdot \boldsymbol{\nabla} p^h d\Omega \quad : \tilde{\gamma}_{\mathrm{v}}, \tag{3.43}$$

$$\beta: \quad \int_{\Omega_e} \boldsymbol{\nabla} q^h \cdot \frac{\partial \mathbf{u}^h}{\partial t} d\Omega \quad : \beta_{\mathrm{v}}, \tag{3.44}$$

$$\gamma: \quad \int_{\Omega_e} \boldsymbol{\nabla} q^h \cdot (\mathbf{u}^h \cdot \boldsymbol{\nabla}\mathbf{u}^h) d\Omega \quad : \gamma_{\mathrm{v}}, \tag{3.45}$$

$$\theta: \quad \int_{\Omega_e} \boldsymbol{\nabla} q^h \cdot \boldsymbol{\nabla} p^h d\Omega \quad : \theta_{\mathrm{v}}, \tag{3.46}$$

$$\mathbf{e}: \quad \int_{\Omega_e} (\boldsymbol{\nabla} \cdot \mathbf{w}^h) \rho (\boldsymbol{\nabla} \cdot \mathbf{u}^h) d\Omega \quad : \mathbf{e}_{\mathrm{v}}. \tag{3.47}$$

The following element-level matrices and vectors $\mathbf{c}_{\mathrm{r}}$, $\tilde{\mathbf{k}}_{\mathrm{r}}$, $(\mathbf{c}_{\mathrm{r}})_{\mathrm{v}}$, and $(\tilde{\mathbf{k}}_{\mathrm{r}})_{\mathrm{v}}$ from [24] are used to define the diffusive limit of τ:

$$\mathbf{c}_{\mathrm{r}}: \quad \int_{\Omega^e} \mathbf{w}^h \cdot \rho(\mathbf{r} \cdot \boldsymbol{\nabla}\mathbf{u}^h) d\Omega \quad : (\mathbf{c}_{\mathrm{r}})_{\mathrm{v}}\ , \tag{3.48}$$

$$\tilde{\mathbf{k}}_{\mathrm{r}}: \quad \int_{\Omega^e} (\mathbf{r} \cdot \boldsymbol{\nabla}\mathbf{w}^h) \cdot \rho(\mathbf{r} \cdot \boldsymbol{\nabla}\mathbf{u}^h) d\Omega \quad : (\tilde{\mathbf{k}}_{\mathrm{r}})_{\mathrm{v}}\ . \tag{3.49}$$

All applicable remarks from [30] still apply for the Navier–Stokes equation for incompressible flows.

The element-level Reynolds and Courant numbers are defined the same way as they were defined before, as given by Eqs. (3.24)-(3.27). The components of the element-matrix-based τ_{SUPG} are defined the same way as they were defined before, as given by Eqs. (3.28)-(3.30). τ_{SUPG} is constructed from its components the same way as it was constructed before, as give by Eq. (3.31). The components of the element-vector-based τ_{SUPG} are defined the same way as they were defined before, as given by Eqs. (3.32)-(3.34). The construction of $(\tau_{\text{SUPG}})_{\text{V}}$ is also the same as it was before, given by Eq. (3.35).

The components of the element-matrix-based τ_{PSPG} are defined as follows [30, 24]:

$$\tau_{\text{P1}} = \frac{\|\mathbf{g}^{\text{T}}\|}{\|\gamma\|}, \tag{3.50}$$

$$\tau_{\text{P2}} = \frac{\Delta t}{2}\frac{\|\mathbf{g}^{\text{T}}\|}{\|\beta\|}, \tag{3.51}$$

$$\tau_{\text{P3}} = \tau_{\text{P1}}\frac{\|\mathbf{c}\|}{\nu\,\|\tilde{\mathbf{k}}_{\text{r}}\|} \quad \text{or} \quad \tau_{\text{P1}}\,Re\left(\frac{h_{\text{RGN}}}{h_{\text{UGN}}}\right)^2. \tag{3.52}$$

τ_{PSPG} is constructed from its components as follows:

$$\tau_{\text{PSPG}} = \left(\frac{1}{\tau_{\text{P1}}^r} + \frac{1}{\tau_{\text{P2}}^r} + \frac{1}{\tau_{\text{P3}}^r}\right)^{-\frac{1}{r}}. \tag{3.53}$$

The components of the element-vector-based τ_{PSPG} are defined as follows [30, 24]:

$$\tau_{\text{PV1}} = \tau_{\text{P1}}, \tag{3.54}$$

$$\tau_{\text{PV2}} = \tau_{\text{PV1}}\frac{\|\gamma_{\text{V}}\|}{\|\beta_{\text{V}}\|}, \tag{3.55}$$

$$\tau_{\text{PV3}} = \tau_{\text{PV1}}\frac{\|\mathbf{c}\|}{\nu\,\|\tilde{\mathbf{k}}_{\text{r}}\|} \quad \text{or} \quad \tau_{\text{PV1}}\,Re\left(\frac{h_{\text{RGN}}}{h_{\text{UGN}}}\right)^2. \tag{3.56}$$

With these components,

$$(\tau_{\text{PSPG}})_{\text{V}} = \left(\frac{1}{\tau_{\text{PV1}}^r} + \frac{1}{\tau_{\text{PV2}}^r} + \frac{1}{\tau_{\text{PV3}}^r} \right)^{-\frac{1}{r}}. \tag{3.57}$$

The element-matrix-based ν_{LSIC} is defined as follows [30]:

$$\nu_{\text{LSIC}} = \frac{\|\mathbf{c}\|}{\|\mathbf{e}\|}. \tag{3.58}$$

We define the element-vector-based ν_{LSIC} to be identical to the element-matrix-based ν_{LSIC}:

$$(\nu_{\text{LSIC}})_{\text{V}} = \nu_{\text{LSIC}}. \tag{3.59}$$

3.4.2 DSD/SST Formulation

For extensions of the τ calculations based on matrix norms, we define the space–time augmented versions of the element-level matrices and vectors given by Eqs. (3.37), (3.41), and (3.45):

$$\mathbf{c}_{\text{A}} : \qquad \int_{Q_n^e} \mathbf{w}^h \cdot \rho \left(\frac{\partial \mathbf{u}^h}{\partial t} + \mathbf{u}^h \cdot \boldsymbol{\nabla} \mathbf{u}^h \right) dQ \qquad : (\mathbf{c}_{\text{A}})_{\text{V}}, \tag{3.60}$$

$$\tilde{\mathbf{k}}_{\text{A}} : \quad \int_{Q_n^e} \left(\frac{\partial \mathbf{w}^h}{\partial t} + \mathbf{u}^h \cdot \boldsymbol{\nabla} \mathbf{w}^h \right) \cdot \rho \left(\frac{\partial \mathbf{u}^h}{\partial t} + \mathbf{u}^h \cdot \boldsymbol{\nabla} \mathbf{u}^h \right) dQ \quad : (\tilde{\mathbf{k}}_{\text{A}})_{\text{V}}, \tag{3.61}$$

$$\gamma_{\text{A}} : \qquad \int_{Q_n^e} \boldsymbol{\nabla} q^h \cdot \left(\frac{\partial \mathbf{u}^h}{\partial t} + \mathbf{u}^h \cdot \boldsymbol{\nabla} \mathbf{u}^h \right) dQ \qquad : (\gamma_{\text{A}})_{\text{V}}. \tag{3.62}$$

The components of element-matrix-based τ_{SUPG} are defined as follows:

$$\tau_{\text{S12}} = \frac{\|\mathbf{c}_{\text{A}}\|}{\|\tilde{\mathbf{k}}_{\text{A}}\|}, \tag{3.63}$$

$$\tau_{\text{S3}} = \tau_{\text{S12}} \frac{\|\mathbf{c}_{\text{A}}\|}{\nu \, \|\tilde{\mathbf{k}}_{\text{r}}\|}, \tag{3.64}$$

where $\tilde{\mathbf{k}}_{\mathrm{r}}$ is the space–time version (i.e. integrated over the space–time element domain Q_n^e) of the element-level matrix given by Eq. (3.49). To construct τ_{SUPG} from its components we propose the form

$$\tau_{\mathrm{SUPG}} = \left(\frac{1}{\tau_{\mathrm{S12}}^r} + \frac{1}{\tau_{\mathrm{S3}}^r} \right)^{-\frac{1}{r}}. \tag{3.65}$$

The components of the element-vector-based τ_{SUPG} are defined as follows:

$$\tau_{\mathrm{SV12}} = \frac{\|(\mathbf{c}_{\mathrm{A}})_{\mathrm{V}}\|}{\|(\tilde{\mathbf{k}}_{\mathrm{A}})_{\mathrm{V}}\|}, \tag{3.66}$$

$$\tau_{\mathrm{SV3}} = \tau_{\mathrm{SV12}} \frac{\|\mathbf{c}_{\mathrm{A}}\|}{\nu \, \|\tilde{\mathbf{k}}_{\mathrm{r}}\|}. \tag{3.67}$$

From these two components,

$$(\tau_{\mathrm{SUPG}})_{\mathrm{V}} = \left(\frac{1}{\tau_{\mathrm{SV12}}^r} + \frac{1}{\tau_{\mathrm{SV3}}^r} \right)^{-\frac{1}{r}}. \tag{3.68}$$

The components of element-matrix-based τ_{PSPG} are defined as follows:

$$\tau_{\mathrm{P12}} = \frac{\|\mathbf{g}^{\mathrm{T}}\|}{\|\gamma_{\mathrm{A}}\|}, \tag{3.69}$$

$$\tau_{\mathrm{P3}} = \tau_{\mathrm{P12}} \frac{\|\mathbf{c}_{\mathrm{A}}\|}{\nu \, \|\tilde{\mathbf{k}}_{\mathrm{r}}\|}, \tag{3.70}$$

where $\mathbf{g}^{\mathrm{T}}$ is the space–time version of the element-level matrix given by Eq. (3.40). To construct τ_{PSPG} from its components we propose the form

$$\tau_{\mathrm{PSPG}} = \left(\frac{1}{\tau_{\mathrm{P12}}^r} + \frac{1}{\tau_{\mathrm{P3}}^r} \right)^{-\frac{1}{r}}. \tag{3.71}$$

The components of the element-vector-based τ_{PSPG} are defined as follows:

$$\tau_{\text{PV12}} = \frac{\|\mathbf{g}_{\text{V}}^{\text{T}}\|}{\|(\gamma_{\text{A}})_{\text{V}}\|}, \tag{3.72}$$

$$\tau_{\text{PV3}} = \tau_{\text{PV12}} \frac{\|\mathbf{c}_{\text{A}}\|}{\nu \, \|\tilde{\mathbf{k}}_{\text{r}}\|}. \tag{3.73}$$

From these components,

$$(\tau_{\text{PSPG}})_{\text{V}} = \left(\frac{1}{\tau_{\text{PV12}}^{r}} + \frac{1}{\tau_{\text{PV3}}^{r}} \right)^{-\frac{1}{r}}. \tag{3.74}$$

The element-matrix-based ν_{LSIC} is defined as

$$\nu_{\text{LSIC}} = \frac{\|\mathbf{c}_{\text{A}}\|}{\|\mathbf{e}\|}, \tag{3.75}$$

where $\mathbf{e}$ is the space–time version of the element-level matrix given by Eq. (3.47).

The element-vector-based ν_{LSIC} is defined as

$$(\nu_{\text{LSIC}})_{\text{V}} = \nu_{\text{LSIC}}. \tag{3.76}$$

Chapter 4

Comparison of Stabilization Parameters

This chapter compares the currently-used stabilization parameter for the SUPG, PSPG, and LSIC stabilizations (abbreviated as UGN) to the element-matrix-based (EMB) and element-vector-based (EVB) stabilization parameters. First, a detailed analysis of each stabilization component is presented for UGN and EMB definitions of τ for several different element shapes. Then, this chapter provides additional analysis of degenerated elements to show the impact of degeneration on τ when calculated using element-level matrices and vectors. Additionally, a visualization of the currently-used stabilization parameters for the space–time formulation provides a representation of τ.

4.1 Element Shape Comparison

For these comparisons, the UGN stabilization parameters, calculated using Equations (3.1),(3.2), (3.9), and (3.10), and EMB parameters are calculated for a given shape. This thesis focuses on quadrilateral and triangular elements, for a variety of shapes. The following are a sampling of four quadrilateral shapes and three trian-

gular shapes, with additional testing on certain cases: a square, a rectangle (shown with aspect ratio 2), a parallelogram, and a trapezoid, a right isosceles triangle, a right triangle, and an equilateral triangle. Figures 4.1 and 4.2 show examples of the elements tested.

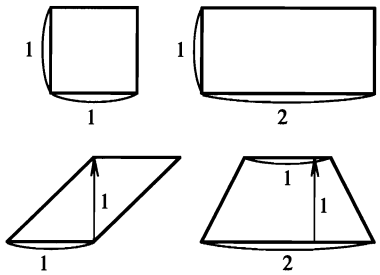

Figure 4.1: Quadrilateral elements used for numerical tests with 2D element shapes. A square (upper-left), a rectangle with aspect ratio 2 (upper-right), a parallelogram (lower-left), and a trapezoid (lower-right).

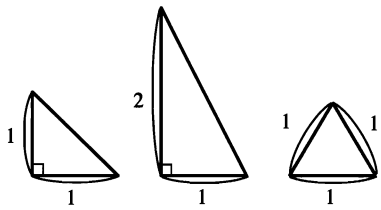

Figure 4.2: Triangular elements used for numerical tests with 2D element shapes. A right isosceles triangle (left), a right triangle (middle), and an equilateral triangle (right).

In order to verify the correct calculation of all versions of the stabilization parameters, the chapter ensures compatibility with the results reported in [30] and then expands on the investigation of the parameters. For this problem, $\|\mathbf{u}^h\| = 1$, $\Delta t = 1$, and the flow direction varies from 0 to 360 degrees at equal intervals. Based on these parameters, the results shown not only directly represent τ_{SUGN1}, but also provide a representation of the element length from Equation (3.4). In the EMB and EVB results reported here, we use the 1-norm.

4.1.1 SUPG and PSPG Stabilization Parameters

First, we will focus on the stabilization parameters for the SUPG and PSPG stabilizations. The SUPG stabilization for UGN-based τ has three components, of which only two are evaluated in this study. The PSPG stabilization parameter for UGN-based τ is set equal to the SUPG stabilization parameter. For the EMB stabilization parameters, the PSPG parameters are calculated using matrix norms. Therefore, the SUPG and PSPG element shape comparisons show the UGN-based τ (representing both SUPG and PSPG), the EMB SUPG stabilization parameter, and the EMB PSPG stabilization parameter. Figures 4.3 and 4.4 show the results for τ_{SUGN1}, τ_{S1}, and τ_{P1} for quadrilateral and triangular elements, respectively.

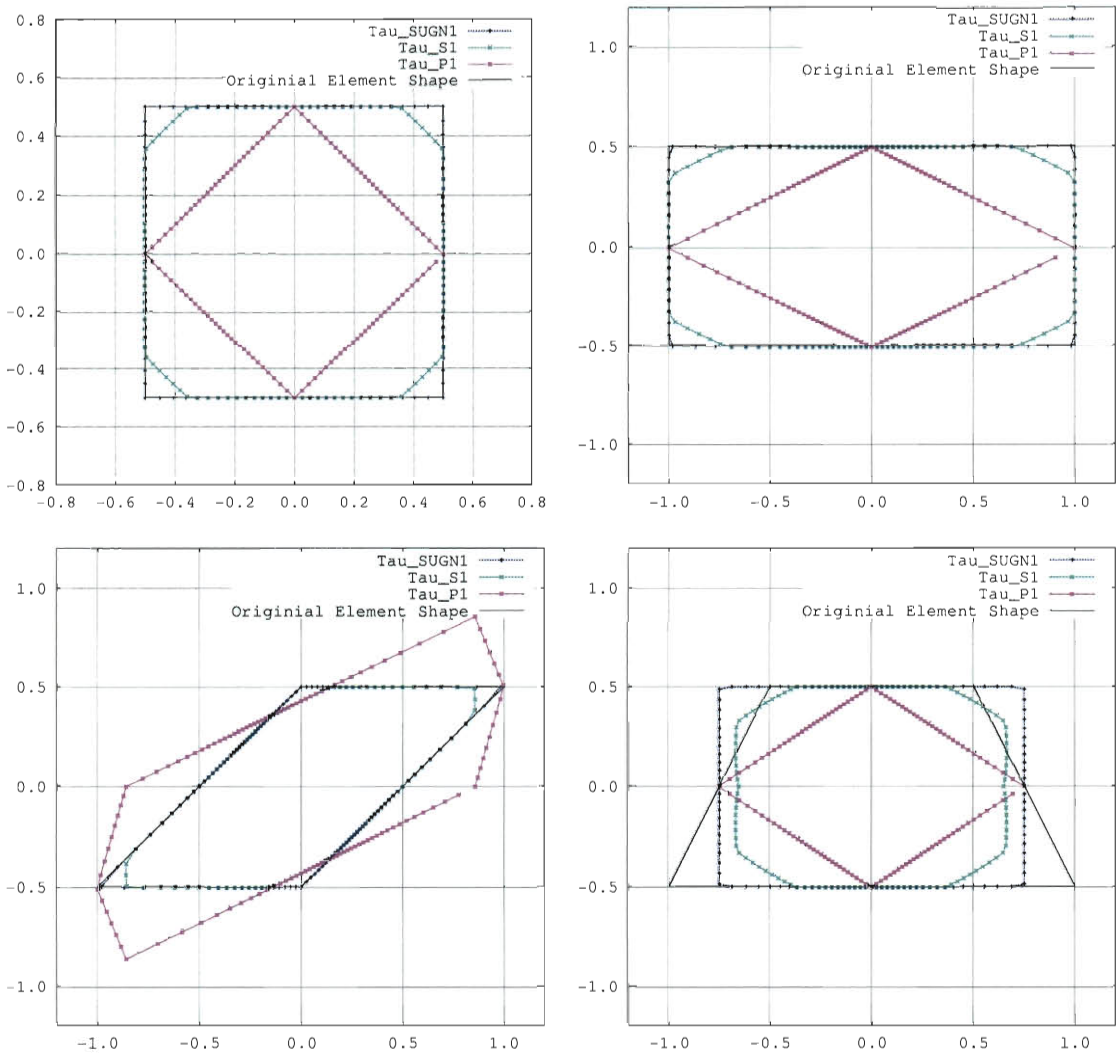

Figure 4.3: Stabilization parameters τ_{SUGN1}, τ_{S1}, and τ_{P1} for quadrilateral elements. A square (upper-left), a rectangle with aspect ratio 2 (upper-right), a parallelogram (lower-left), and a trapezoid (lower-right).

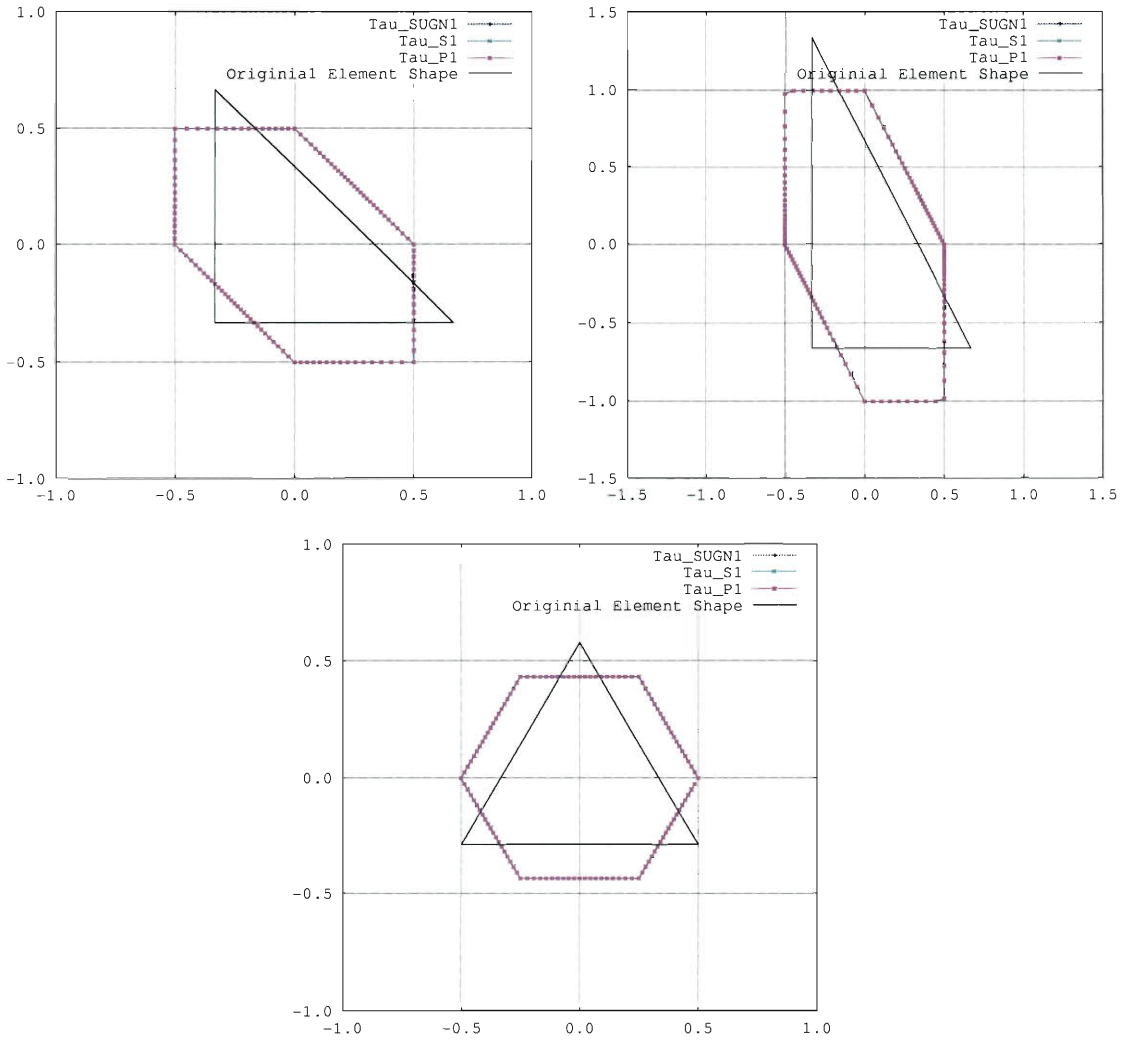

Figure 4.4: Stabilization parameters τ_{SUGN1}, τ_{S1}, and τ_{P1} for triangular elements. A right isosceles triangle (upper-left), a right triangle (upper-right), and an equilateral triangle (lower).

As shown in Figure 4.4, τ_{SUGN1}, τ_{S1}, and τ_{P1} are equal for triangular elements.

Figures 4.5 and 4.6 show the results for τ_{SUGN2}, τ_{S2}, and τ_{P2} for quadrilateral and triangular elements, respectively.

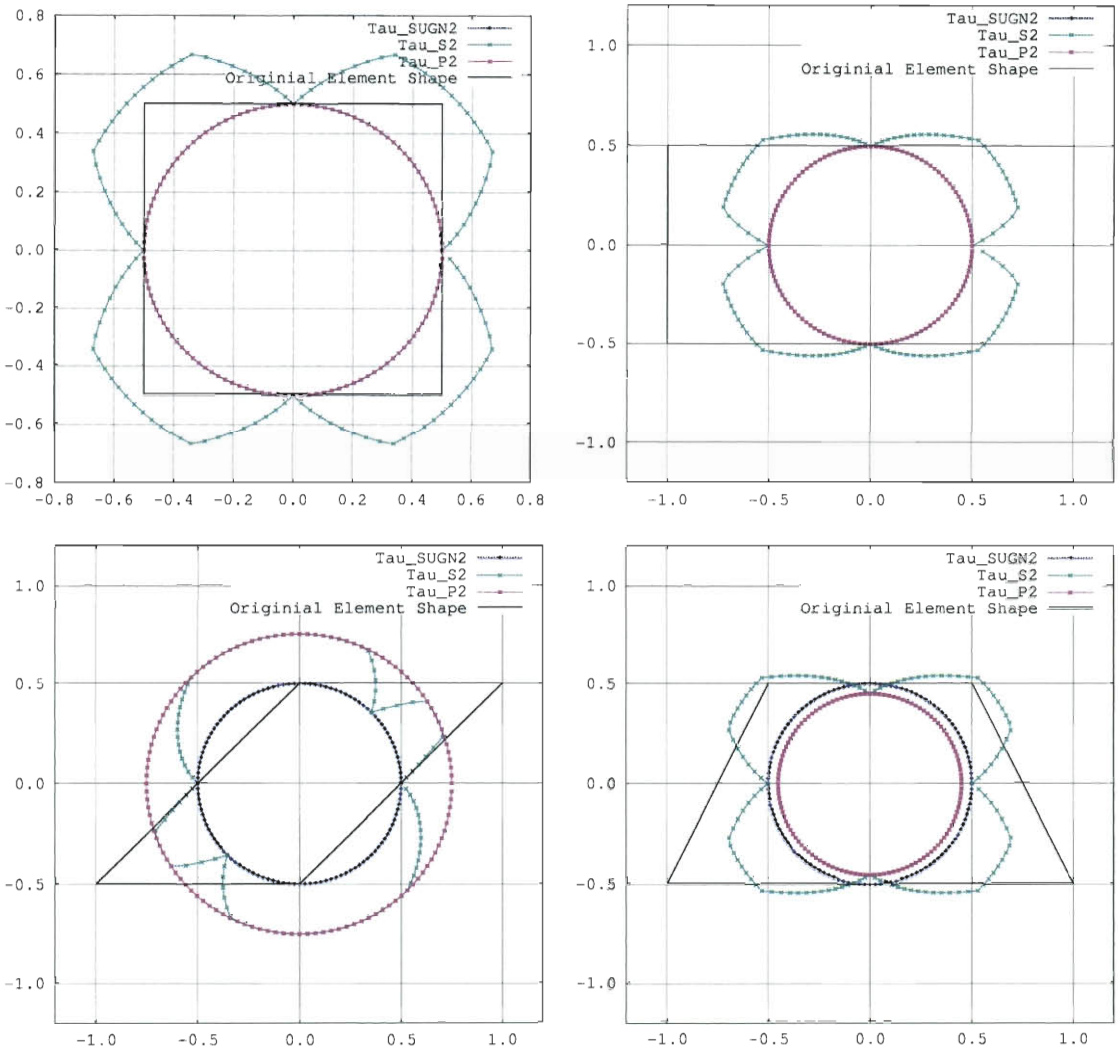

Figure 4.5: Stabilization parameters τ_{SUGN2}, τ_{S2}, and τ_{P2} for quadrilateral elements. A square (upper-left), a rectangle with aspect ratio 2 (upper-right), a parallelogram (lower-left), and a trapezoid (lower-right).

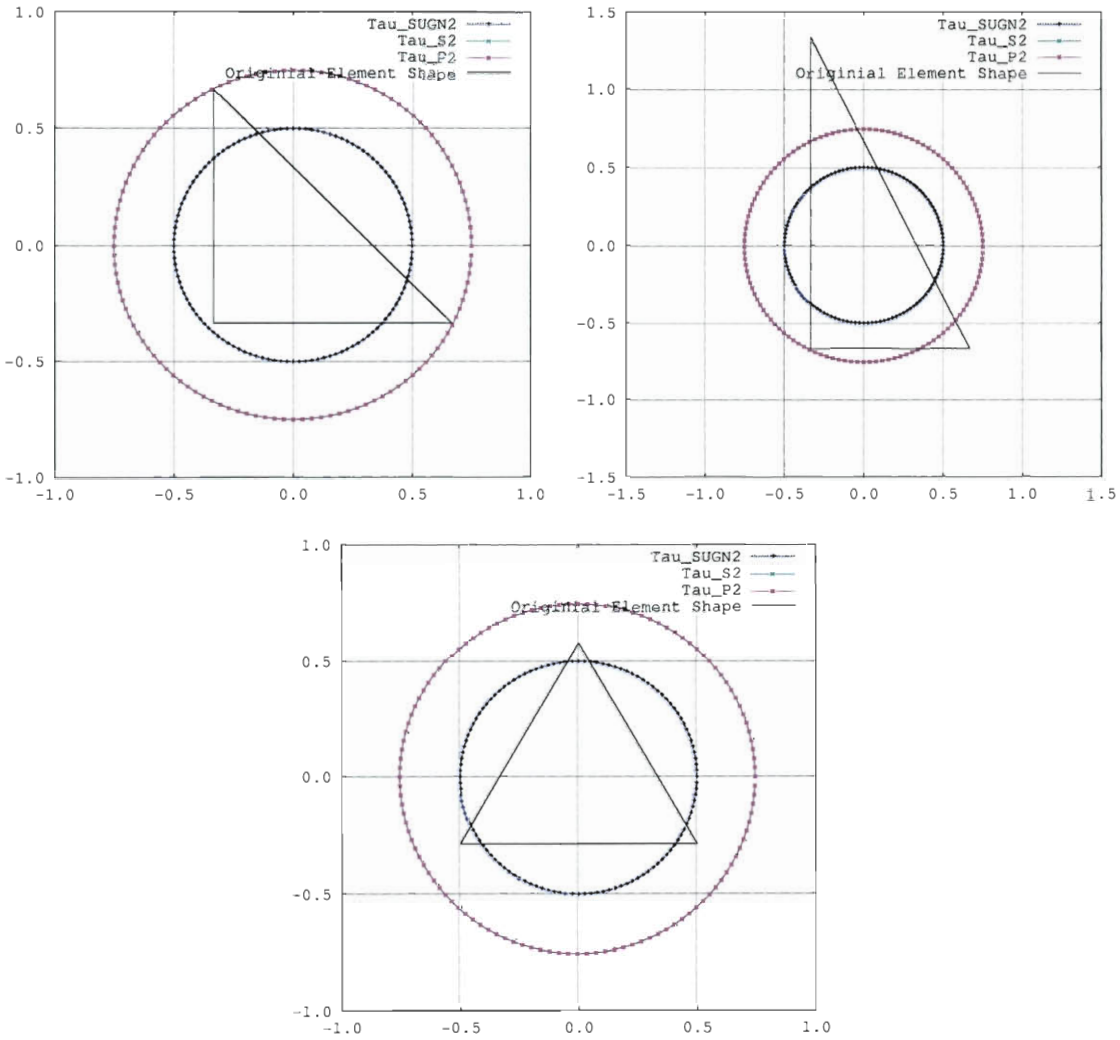

Figure 4.6: Stabilization parameters τ_{SUGN2}, τ_{S2}, and τ_{P2} for triangular elements. A right isosceles triangle (upper-left), a right triangle (upper-right), and an equilateral triangle (lower).

All stabilization parameters shown thus far match the results reported in [30].

4.1.2 LSIC Stabilization Parameters

Next, the UGN LSIC stabilization parameter, defined by Equation (3.10), is compared to the EMB LSIC parameter. For both UGN and EMB stabilization parameters, ν_{LSIC} is also compared for the shapes given in Figures 4.1 and 4.2. The results are shown in Figures 4.7 and 4.8 for quadrilateral and triangular elements, respectively.

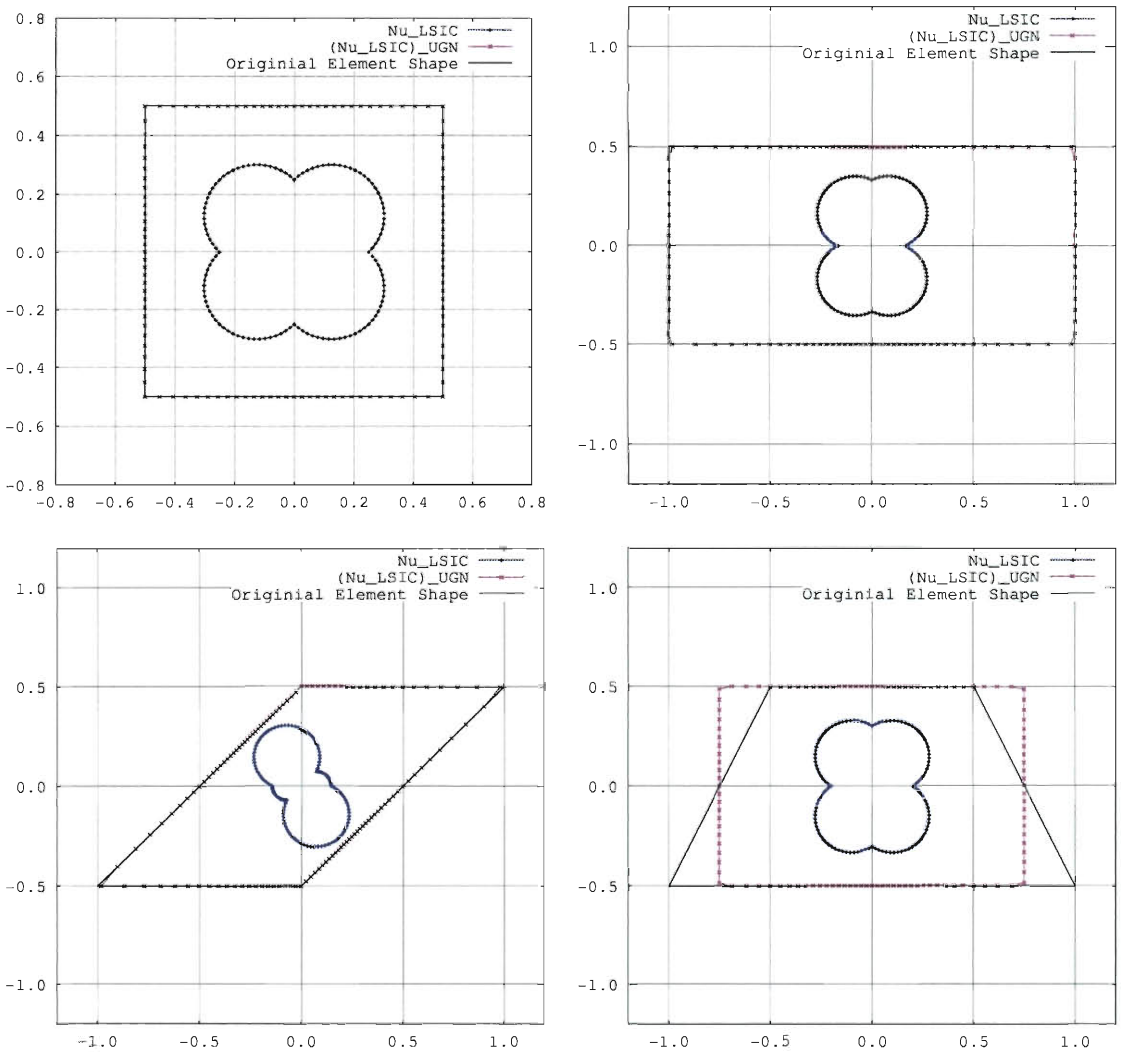

Figure 4.7: Stabilization parameters $(\nu_{\text{LSIC}})_{\text{UGN}}$ and ν_{LSIC} for quadrilateral elements. A square (upper-left), a rectangle with aspect ratio 2 (upper-right), a parallelogram (lower-left), and a trapezoid (lower-right).

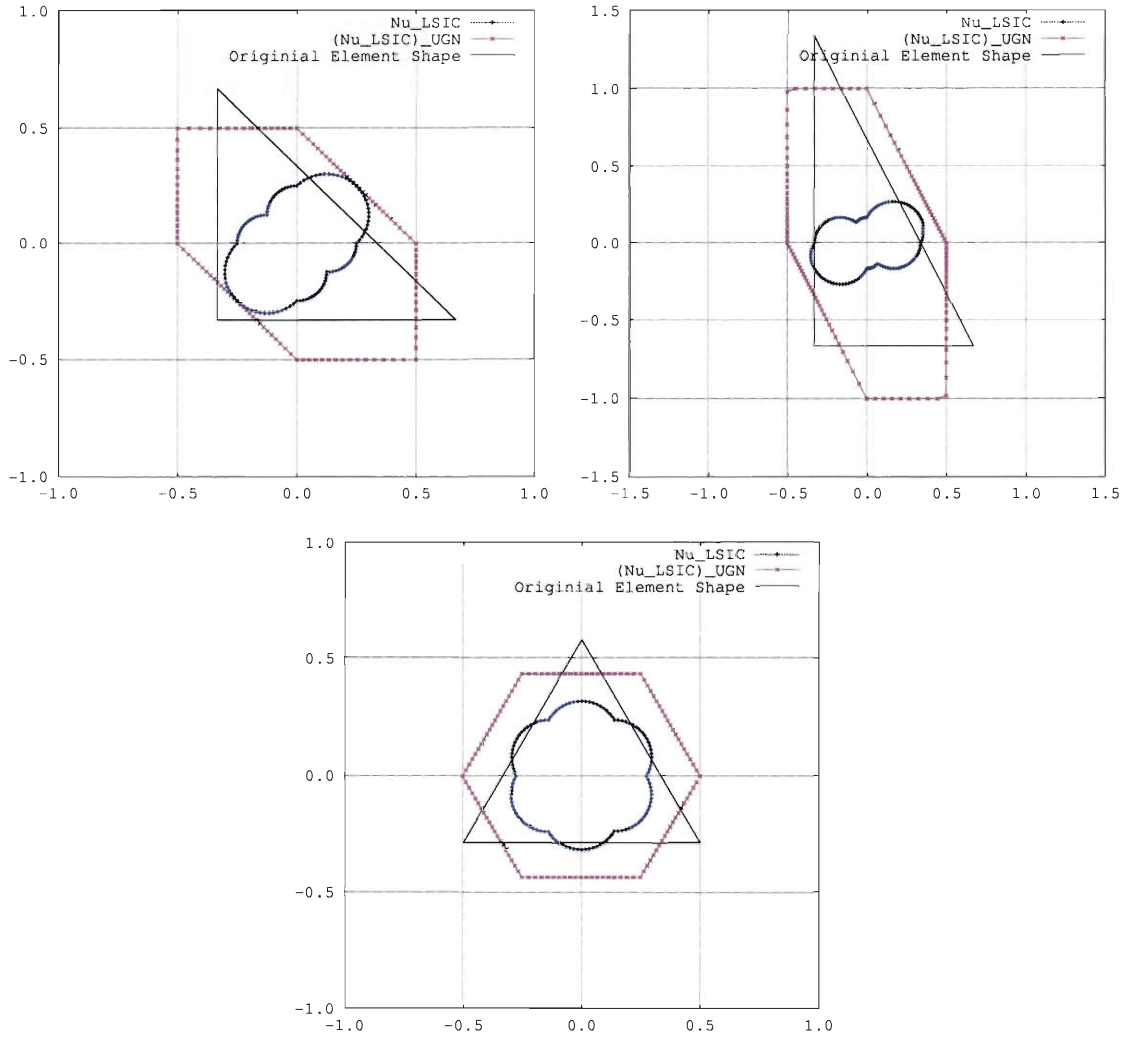

Figure 4.8: Stabilization parameters $(\nu_{\text{LSIC}})_{\text{UGN}}$ and ν_{LSIC} for triangular elements. A right isosceles triangle (upper-left), a right triangle (upper-right), and an equilateral triangle (lower).

We note that for high aspect ratio elements, the EMB ν_{LSIC} is rather detached from the element length, more so for high aspect-ratio elements. Figure 4.9 shows a comparison of square and rectangular elements, where it is apparent that ν_{LSIC} does not represent the higher aspect ratio of the rectangle in the horizontal direction. Analysis of other potential ratios of the matrix norms that might have provided an equivalent estimation to its UGN counterpart yielded no successful replacement to adequately take into account the aspect ratio of the element. Additionally, the EMB ν_{LSIC} plots

calculated here did not match exactly the data presented in [30]. Figure 4.10 shows the equilateral triangle plot, which shows the most evident differences, reported in [30] and the most recent calculation.

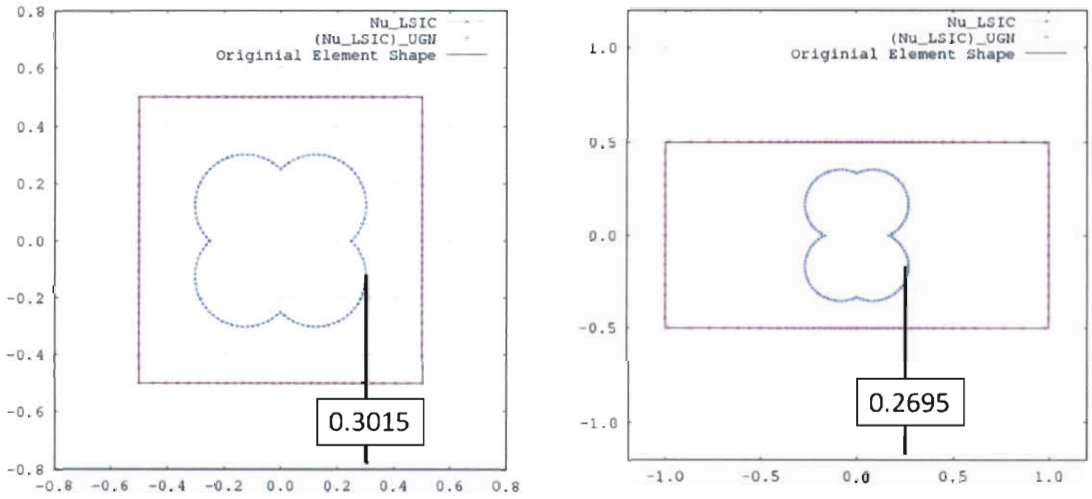

Figure 4.9: Stabilization parameters $(\nu_{\text{LSIC}})_{\text{UGN}}$ and ν_{LSIC} for two quadrilateral elements to emphasize error in high aspect ratio elements. A square (left), and a rectangle with aspect ratio 2 (right). The marked values correspond to a flow direction of approximately 30°.

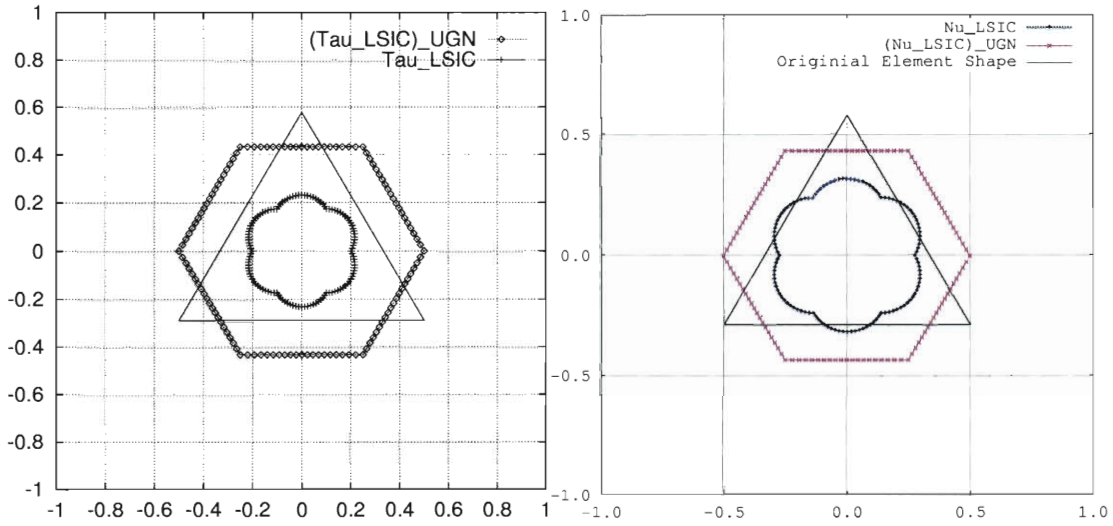

Figure 4.10: Stabilization parameters $(\nu_{\text{LSIC}})_{\text{UGN}}$ and ν_{LSIC} for equilateral triangle. The plot from [30] (left), and the re-calculated plot from this thesis (right).

For these reasons, shown in Figures 4.9 and 4.10, no further investigation of ν_{LSIC} is reported in this thesis.

4.1.3 Element Degeneration

This study of element shapes expands to incorporate element degeneration, specifically a quadrilateral degeneration to a triangle. For quadrilateral elements that degenerate into a triangular shape, an element degeneration technique can be applied to the stabilization parameters to account for the degenerated shape of the element. Figures 4.11 and 4.12 show a quadrilateral element in which degeneration is occurring up to the point that the third and forth nodes are coincident, with τ calculated using the typical quadrilateral interpolation functions and applying the element degeneration technique. This study shows that degeneration techniques can be applied to quadrilateral elements and the impact of degeneration on the calculation of τ for a quadrilateral degeneration to triangular shape.

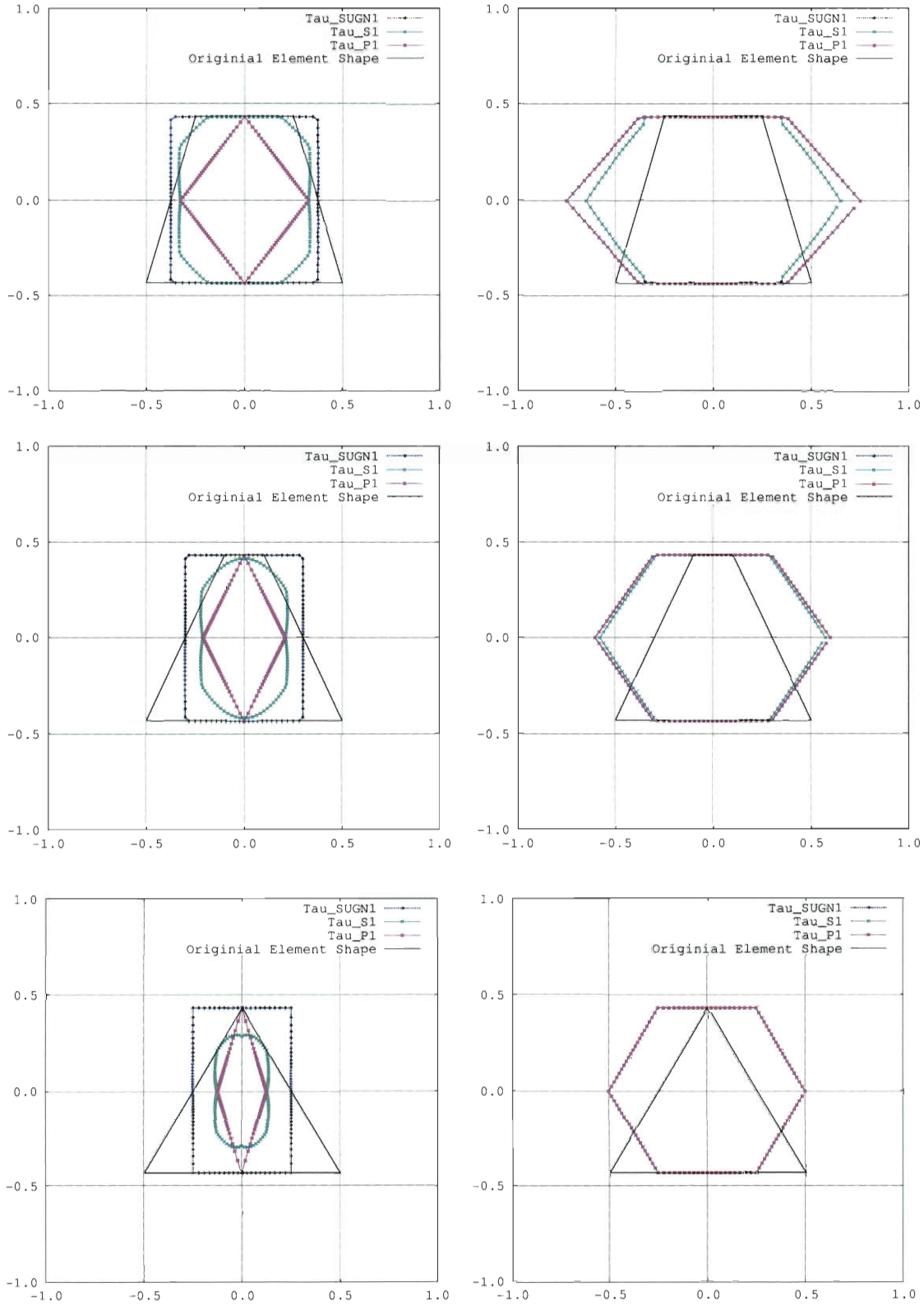

Figure 4.11: Stabilization parameters τ_{SUGN1}, τ_{S1}, and τ_{P1} for a quadrilateral element which is experiencing degeneration to an equilateral triangle. A separation of nodes 3 and 4 of 0.5 (top), 0.2 (middle), and 0.0 units — coincident (bottom). Without

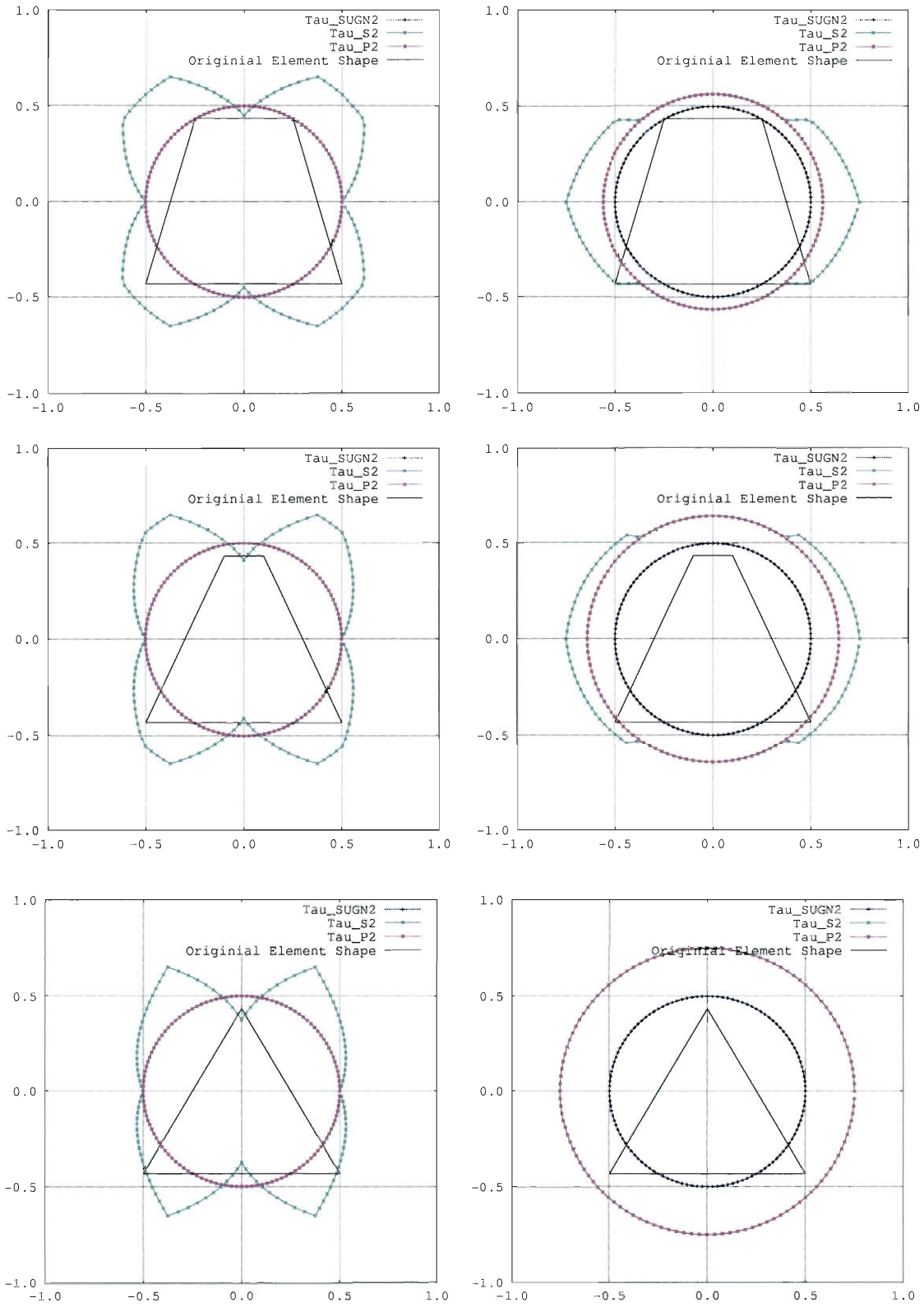

Figure 4.12: Stabilization parameters τ_{SUGN2}, τ_{S2}, and τ_{P2} for a quadrilateral element which is experiencing degeneration to an equilateral triangle. A separation of nodes 3 and 4 of 0.5 (top), 0.2 (middle), and 0.0 units – coincident (bottom). Without

4.2 Space-Time Stabilization Parameter

For these comparisons, the space–time UGN stabilization parameters, calculated using Equations (3.11) and (3.14) are calculated for the shapes given in Figures 4.1 and 4.2. The SUPG stabilization for space–time UGN-based τ has two components, of which only the first is evaluated in this study. The third component of the SUPG stabilization parameter given by Equation (3.3) is not included due to its dependence on the flow field. We assume that there is no mesh motion and the space–time slab Q_n has uniform thickness. The PSPG stabilization parameter for space–time UGN-based τ is set equal to the SUPG stabilization parameter. Therefore, the SUPG and PSPG element shape comparisons shows the space–time UGN-based τ (representing both SUPG and PSPG). Figures 4.13 and 4.14 show the results for τ_{SUGN12} for quadrilateral and triangular elements, respectively.

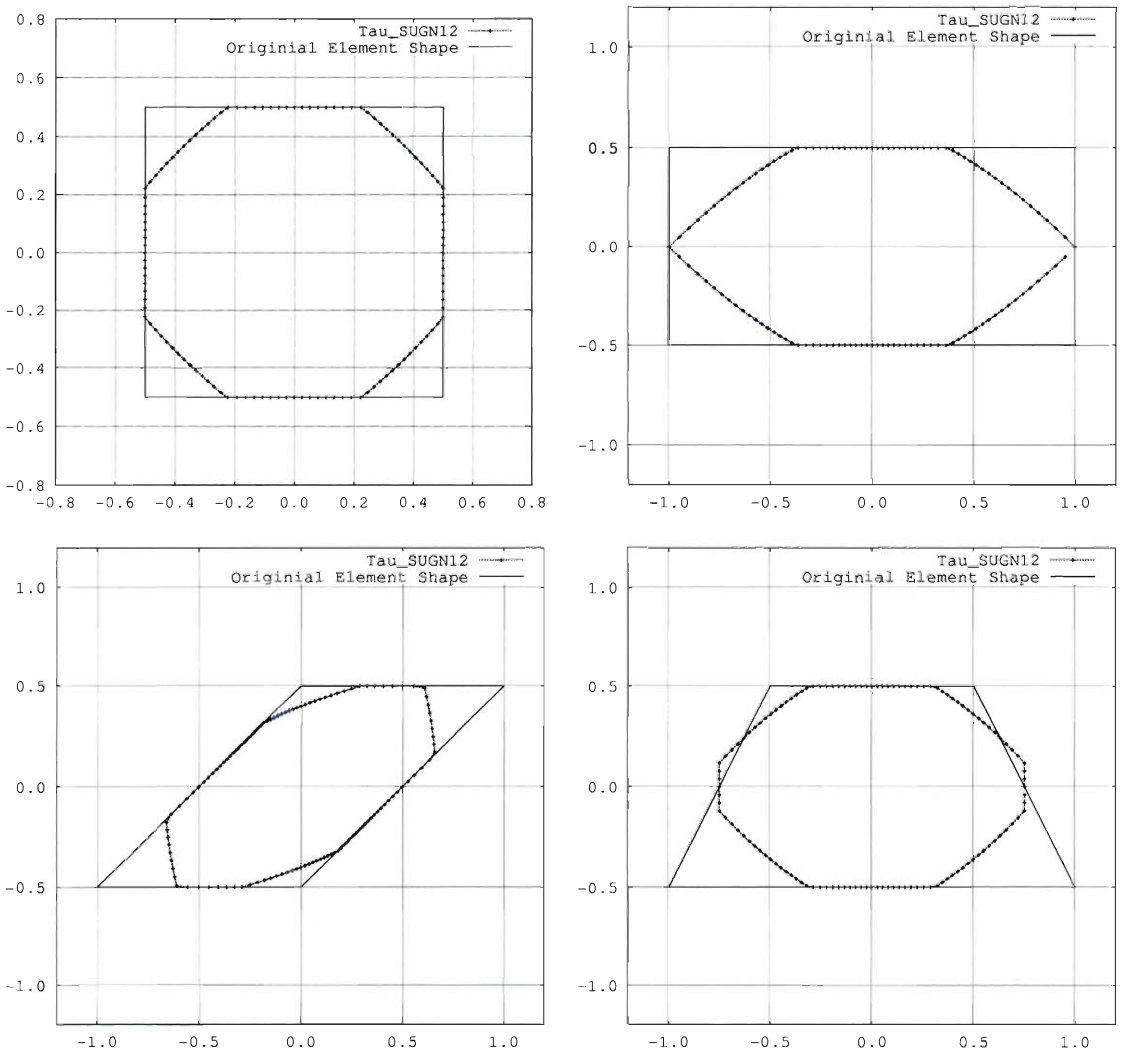

Figure 4.13: Stabilization parameter τ_{SUGN12} for quadrilateral elements. A square (upper-left), a rectangle with aspect ratio 2 (upper-right), a parallelogram (lower-left), and a trapezoid (lower-right).

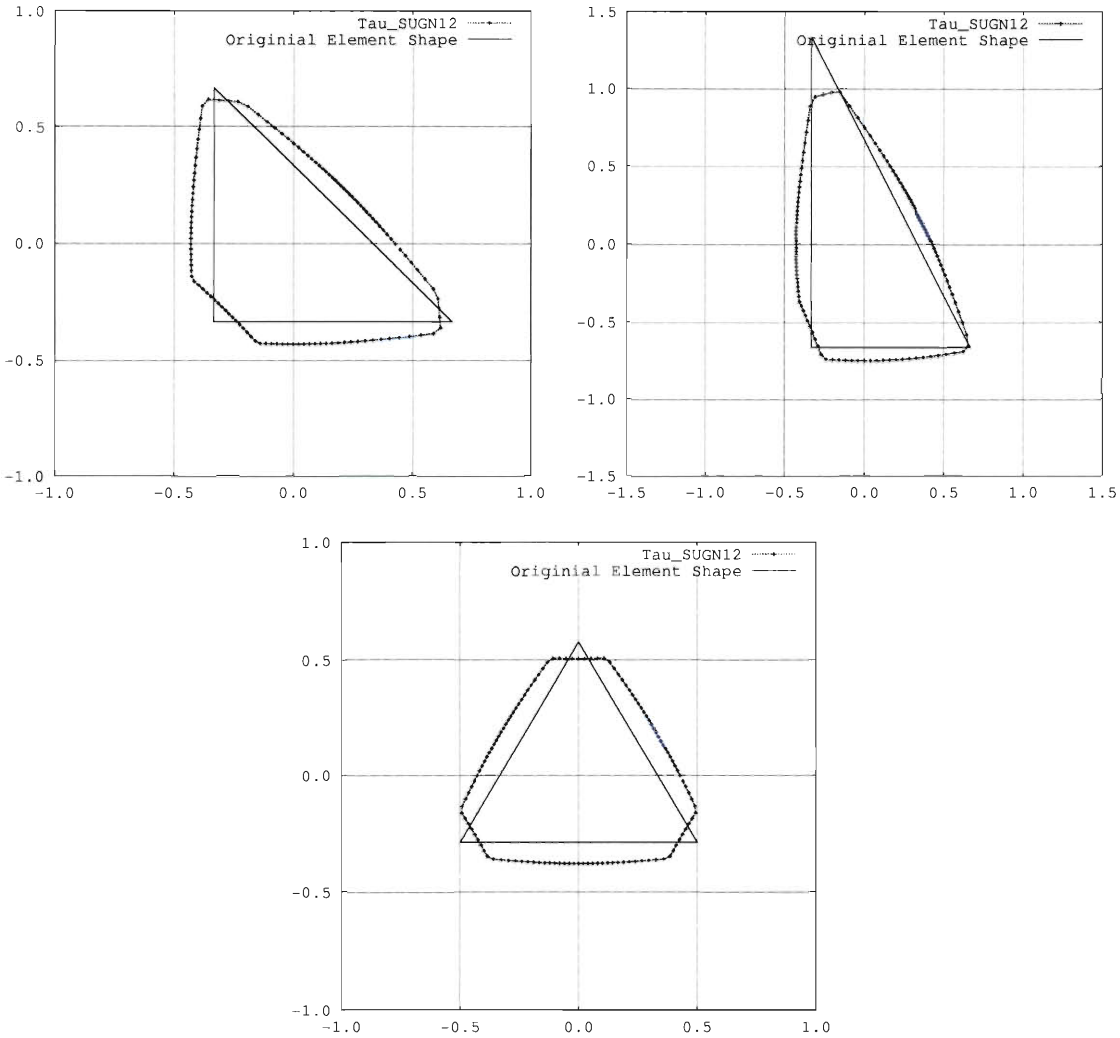

Figure 4.14: Stabilization parameter τ_{SUGN12} for triangular elements. A right isosceles triangle (upper-left), a right triangle (upper-right), and an equilateral triangle (lower).

Chapter 5

Comparison of Stabilization Terms

This chapter compares the impact of different selections of τ on stabilization terms in their assembled form. Currently-used SUPG and PSPG stabilization parameters and the EMB and EVB stabilization parameters are used as part of the assembled stabilization-term matrices of a grouping of elements — varying element type, nodal connectivity, and element distortion. First, two independent analyses are used to study individual matrices, analytically and in an automated program, for quadrilateral and triangular element groupings. To visualize the significance of selection of stabilization parameters across a broad range of element types exhibited in flow applications, the grouping of elements undergoes element distortion, specifically with respect to increasingly large aspect ratio elements often used in the boundary layer. Next, a flow field typically seen in the boundary layer for a no-slip boundary condition is generated to show the impact of different selections of stabilization parameters on each stabilization-term matrix within the system.

5.1 Assembly Comparison

A grouping of the two element types examines the effect of different stabilization parameter selections on assemblies of matrices and determines the variation in results

when using different element types and configurations in the boundary layer. For these tests, four quadrilateral elements and eight triangular elements — generated by splitting each quadrilateral element — provide comparison between element types. The configuration of elements chosen is necessary to enable a direct comparison of the matrices from each element type. Figure 5.1 shows the element configurations tested for quadrilaterals and triangles.

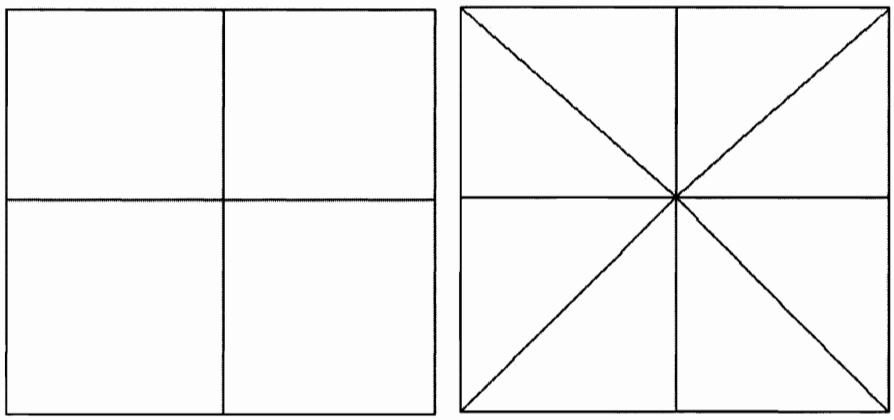

Figure 5.1: Assembly comparison element configurations for quadrilateral (left) and triangular (right) elements.

Two methods are used for the calculation of the assembled stabilization-term matrices. The analytical derivation and manual assembly (ADMA) shows the generalized assembled matrix form, which is valuable to predict the effect of changes in element shape and velocity field on the assembled matrix. The automated calculation and assembly program (ACAP) provides an efficient tool to analyze variations in element shape, configuration, and velocity, once verified analytically by comparing the results to those obtained by the ADMA.

5.1.1 Analytical Derivation and Manual Assembly (ADMA)

The ADMA method for determining each assembled matrix term uses a generalized flow field, $\mathbf{u} = (u, v)$ and a rectangular or triangular element shape, with side lengths

of a and b. Figure 5.2 shows the generalized element groupings for quadrilaterals and triangles.

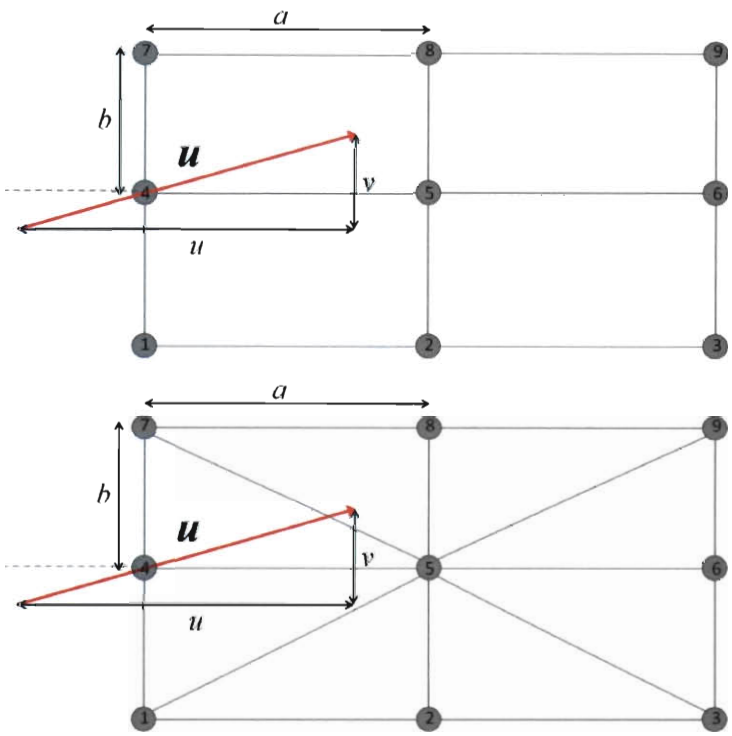

Figure 5.2: Assembly comparison of generalized element configuration using ADMA method for quadrilateral (top) and triangular (bottom) elements.

The analytical matrices for the generalized assembly are shown in Figures 5.3, 5.4, and 5.5 for both quadrilateral and triangular elements. For these cases $\alpha = \frac{u}{a}$ and $\beta = \frac{v}{b}$.

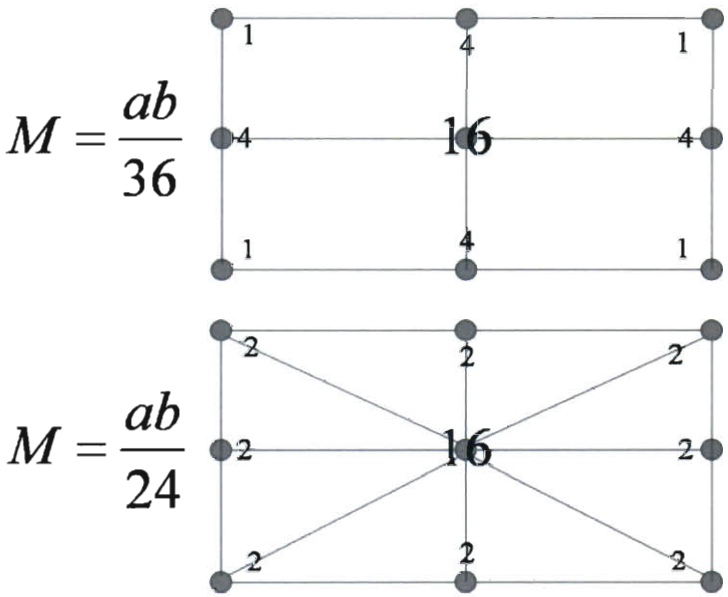

Figure 5.3: Assembled matrix **M** for quadrilateral assembly (upper) and triangular assembly (lower) using ADMA.

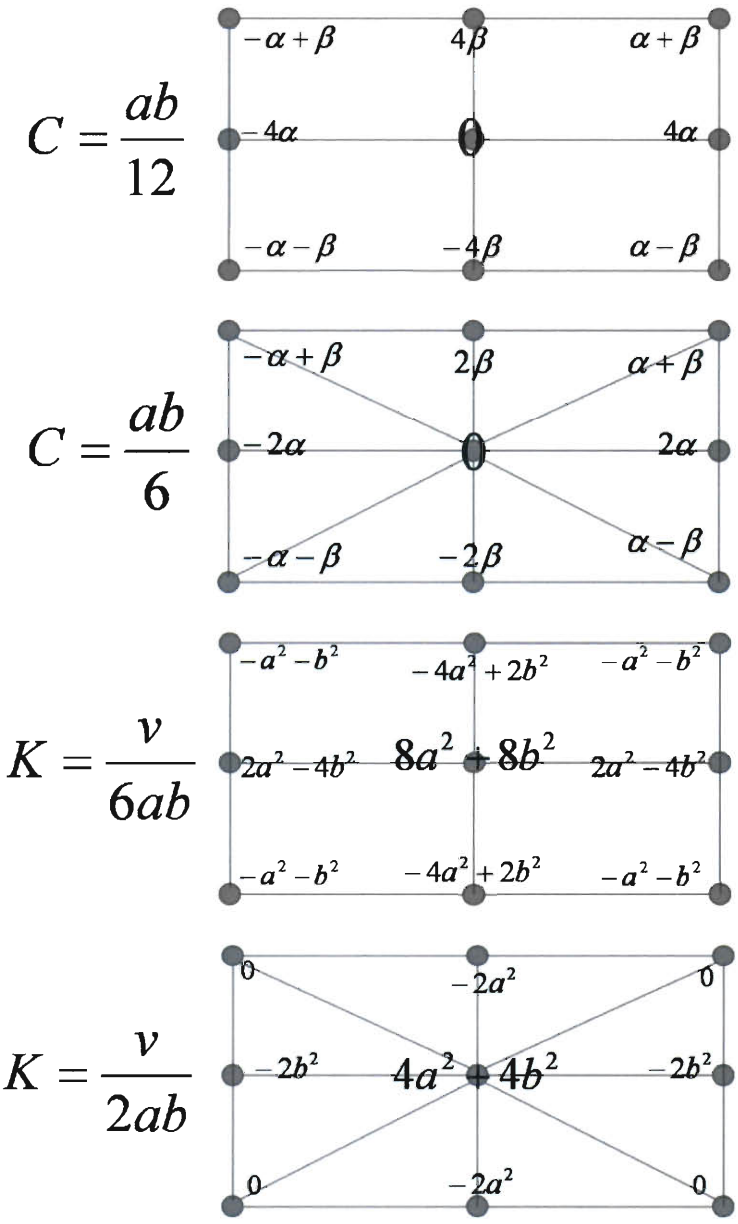

Figure 5.4: Assembled matrices **C** and **K** for quadrilateral assembly (upper) and triangular assembly (lower) using ADMA.

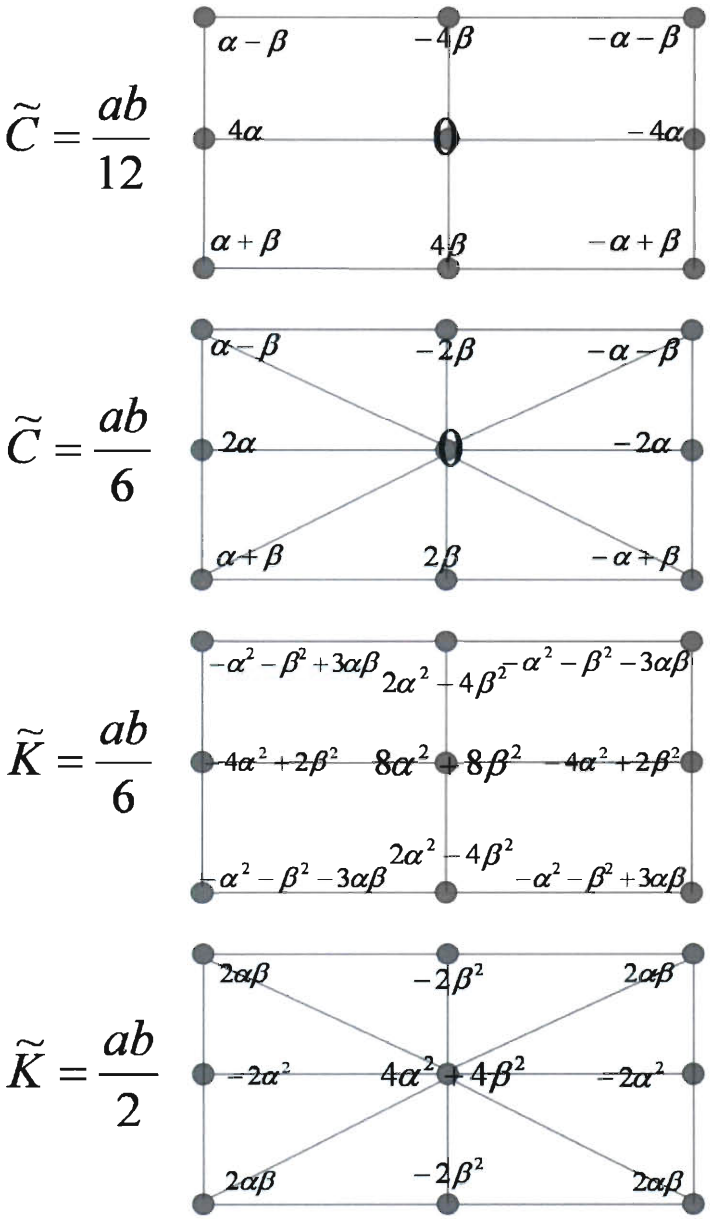

Figure 5.5: Assembled matrices $\tilde{\mathbf{C}}$ and $\tilde{\mathbf{K}}$ for quadrilateral assembly (upper) and triangular assembly (lower) using ADMA.

The relationship between the quadrilateral and triangular elements is notable for these sets of elements. As most easily shown in the case of the **M** matrix, the triangular elements exhibit a more distributed matrix assembly than the quadrilateral elements. This tendency likely comes from the nature of the connectivity for the corner nodes for triangular elements. Generally, the dependencies on element shape and the sign of the terms is consistent independent of element type. The **K** matrix provides a notable exception, in which the assembled matrix for triangles yields zero values at each corner, whereas the quadrilaterals yield non-zero values.

5.1.2 Automated Calculation and Assembly Program (ACAP)

The ACAP allows for variation of the element configurations within each element grouping and provides flexibility with respect to flow field adjustments and element shape.

Various Triangular Element Configurations

Figure 5.6 shows the same quadrilateral and triangular element configurations we studied with the ADMA approach (left) and two additional triangular element configurations (right) for $\mathbf{u} = (1, 0)$.

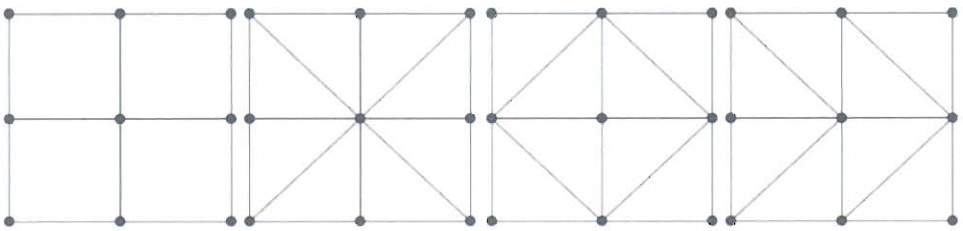

Figure 5.6: Assembly comparison of square shape configurations using ACAP method for quadrilateral element configuration, and three types of triangular element configurations (which we will call T8, T4, and T6).

Figure 5.7 shows individual matrices for all four configurations of elements.

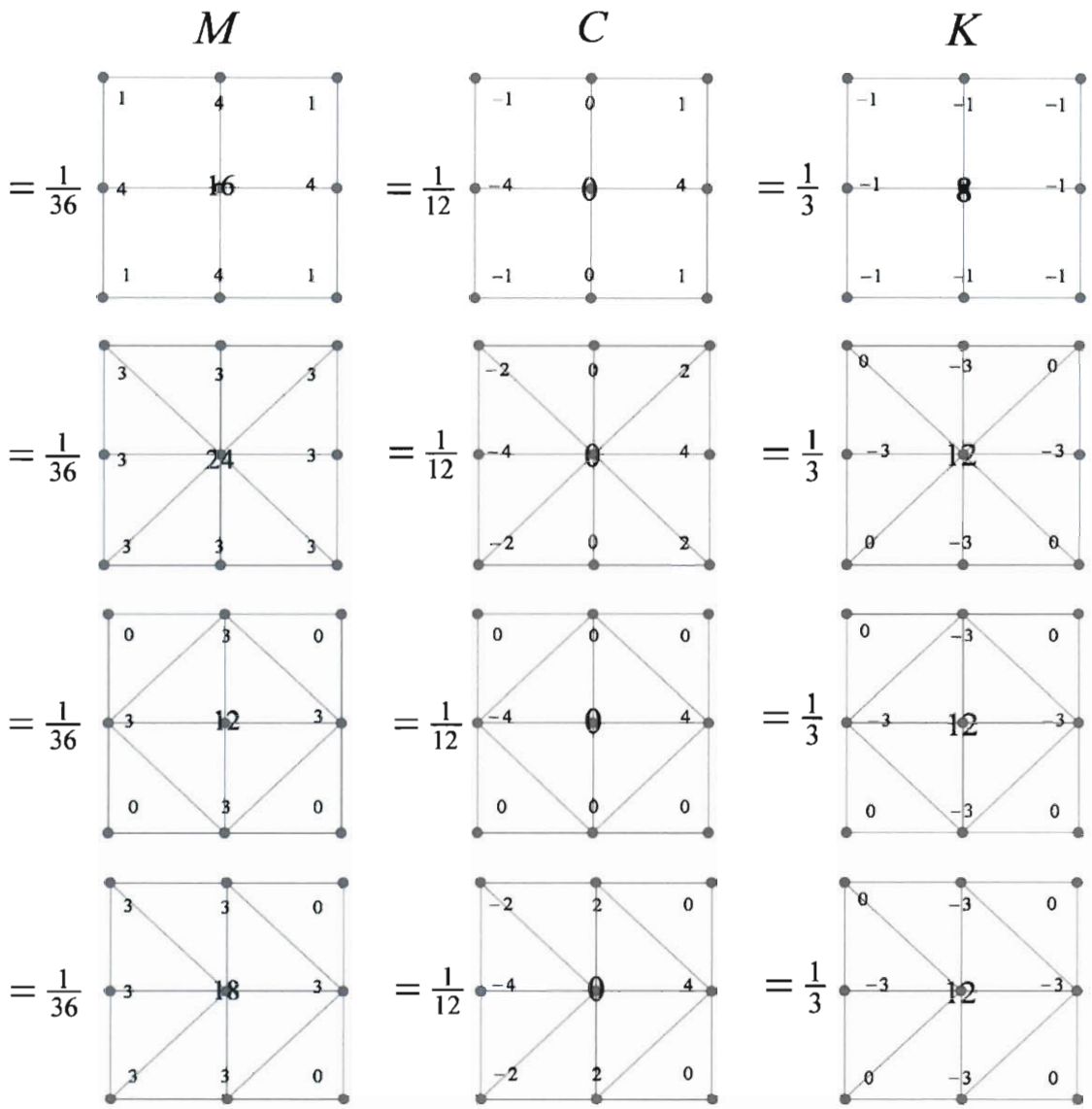

Figure 5.7: Assembled matrices **M**, **C**, and **K** for quadrilateral configuration (top), T8 (upper middle), T4 (lower middle), and T6 (bottom).

Upon inspection, the combination of the T8 and T4 configuration matrices balances the quadrilateral configuration matrices. The T6 configuration provides a reasonable comparison to the rectangular configuration. Generally, triangular elements yield similar results to quadrilateral elements with slight differences depending on the connectivity between nodes.

High Aspect Ratio Elements

Within the boundary layer, a high aspect ratio quadrilateral element is often preferred. Using the ACAP method, the individual matrices are inspected for quadrilateral and triangular element configurations of an aspect ratio 100, such that a=100 and b=1. Figure 5.8 shows the resulting individual matrices for this case for $\mathbf{u} = (1, 0)$.

The differences between quadrilateral and triangular elements are magnified for the high aspect ratio case. For the same conditions, the two element types might yield different results.

5.2 Boundary Flow Cases

This section utilizes the ACAP method to evaluate the impact of different selections of stabilization parameters on stabilization term matrices. A boundary flow is generated from the computation of incompressible flows over a quadrilateral mesh at Re=100. The element height for the first four layers of elements is $.001R$, where R is the cylinder radius. The boundary flow is applied to the quadrilateral and triangular element configurations. By applying a flow field, the stabilization parameters can be determined and compared. Additionally, slight distortion that might be found in boundary elements is applied to the element groupings.

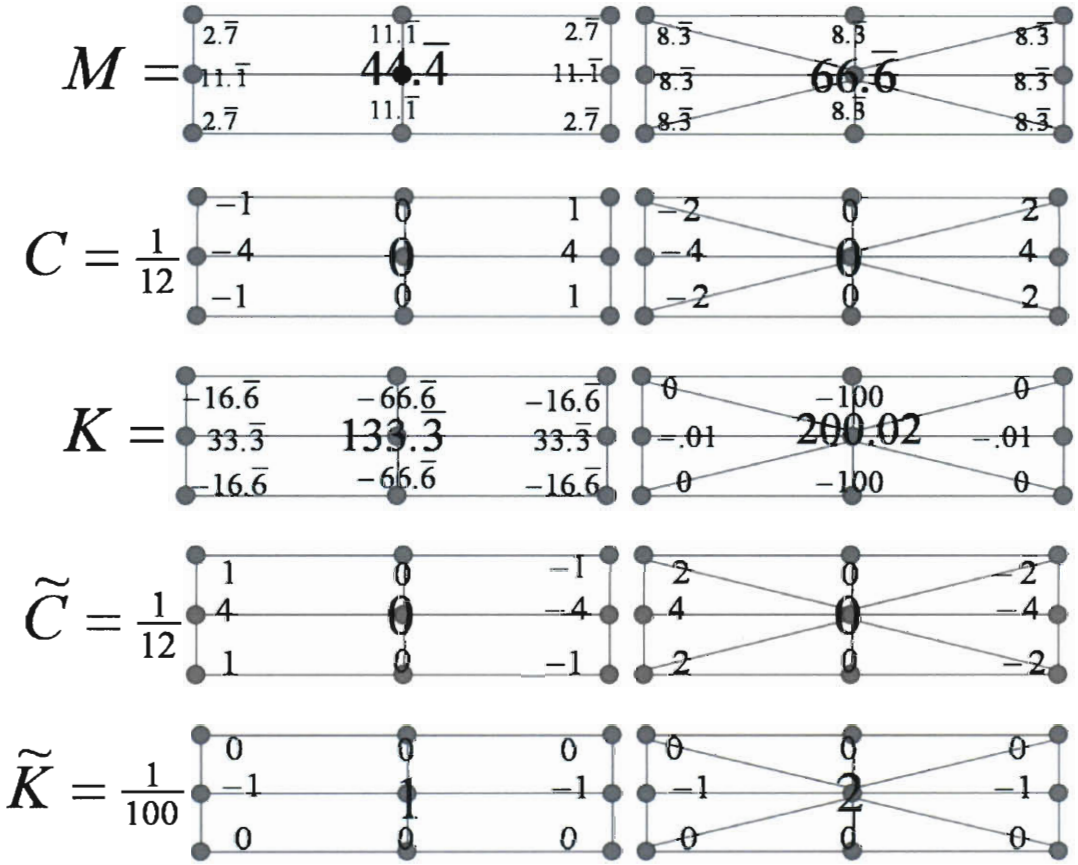

Figure 5.8: Rectangular assembled matrices **M**, **C**, **K**, $\tilde{\mathbf{C}}$, $\tilde{\mathbf{K}}$ for quadrilateral configurations (left) and triangular configurations (right) using ACAP.

5.2.1 Undeformed Element Boundary Flow Assembly

The flow profile extracted from the incompressible flow computation is nearly linear and is shown in Figure 5.9. The velocity profile is typical of that experienced by boundary layer elements with an aspect ratio of 100, tested in Chapter 4 as high aspect ratio elements. A flow field is needed to compare the effect of all τ selections we consider.

In order to show the significance of the differences between each selection of the stabilization parameters, the assembled stabilization terms, $\tilde{\mathbf{C}}$ and $\tilde{\mathbf{K}}$, are multiplied by each τ. Tables 5.1 and 5.2 show quadrilateral element groupings and Tables 5.3

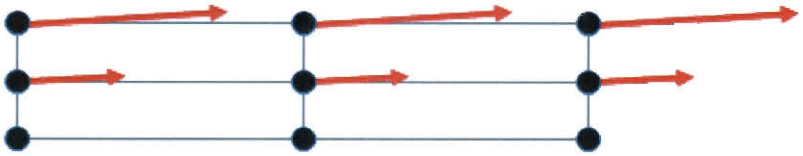

Figure 5.9: Flow field applied on boundary layer elements. These velocity vectors are applied to a generic grouping of elements.

and 5.4 show triangular element groupings.

	7	8	9
$\tilde{C}$	-2.6761e-02	-1.1071e-01	-2.8594e-02
$\tilde{C}\,(\tau_{\text{SUPG}})_{\text{UGN}}$	-1.3380e-02	-5.5355e-02	-1.4297e-02
$\tilde{C}\tau_{\text{SUPG}}$	-1.3823e-02	-5.7188e-02	-1.4770e-02
$\tilde{C}\,(\tau_{\text{SUPG}})_{\text{V}}$	-3.5808e-01	-1.4814e+00	-3.8261e-01
	4	5	6
$\tilde{C}$	-1.5959e-02	-7.3630e-02	-2.0856e-02
$\tilde{C}\,(\tau_{\text{SUPG}})_{\text{UGN}}$	-7.979e-03	-3.6815e-02	-1.0428e-02
$\tilde{C}\tau_{\text{SUPG}}$	-8.2431e-03	-3.8032e-02	-1.0773e-02
$\tilde{C}\,(\tau_{\text{SUPG}})_{\text{V}}$	-8.2349e-02	-4.9314e-01	-1.6422e-01
	1	2	3
$\tilde{C}$	9.5778e-03	3.7080e-02	8.9622e-03
$\tilde{C}\,(\tau_{\text{SUPG}})_{\text{UGN}}$	4.7889e-03	1.8540e-02	4.4811e-03
$\tilde{C}\tau_{\text{SUPG}}$	4.9479e-03	1.9156e-02	4.6299e-03
$\tilde{C}\,(\tau_{\text{SUPG}})_{\text{V}}$	2.5526e-01	9.8824e-01	2.3886e-01

Table 5.1: Assembled matrix ($\tilde{\mathbf{C}}$) and the product of $(\tau_{\text{SUPG}})_{\text{UGN}}$, τ_{SUPG}, and $(\tau_{\text{SUPG}})_{\text{V}}$ for quadrilateral elements.

	7	8	9
$\tilde{K}$	-1.6579e-04	-7.3501e-04	-2.0232e-04
$\tilde{K}\left(\tau_{\text{SUPG}}\right)_{\text{UGN}}$	-8.2893e-05	-3.6750e-04	-1.0116e-04
$\tilde{K}\tau_{\text{SUPG}}$	-8.5638e-05	-3.7967e-04	-1.0451e-04
$\tilde{K}\left(\tau_{\text{SUPG}}\right)_{\text{V}}$	-2.2183e-03	-9.8349e-03	-2.7072e-03
4	5	6	
$\tilde{K}$	2.0403e-04	8.1880e-04	2.0403e-04
$\tilde{K}\left(\tau_{\text{SUPG}}\right)_{\text{UGN}}$	1.0201e-04	4.0940e-04	1.0201e-04
$\tilde{K}\tau_{\text{SUPG}}$	1.0539e-04	4.2296e-04	1.0539e-04
$\tilde{K}\left(\tau_{\text{SUPG}}\right)_{\text{V}}$	3.0031e-03	1.2052e-02	3.0031e-03
1	2	3	
$\tilde{K}$	-2.2701e-05	-8.2451e-05	-1.8592e-05
$\tilde{K}\left(\tau_{\text{SUPG}}\right)_{\text{UGN}}$	-1.1350e-05	-4.1225e-05	-9.2962e-06
$\tilde{K}\tau_{\text{SUPG}}$	-1.1727e-05	-4.2594e-05	-9.6048e-06
$\tilde{K}\left(\tau_{\text{SUPG}}\right)_{\text{V}}$	-6.0502e-04	-2.1974e-03	-4.9552e-04

Table 5.2: Assembled matrix ($\tilde{\mathbf{K}}$) and the product of $(\tau_{\text{SUPG}})_{\text{UGN}}$, τ_{SUPG}, and $(\tau_{\text{SUPG}})_{\text{V}}$ for quadrilateral elements.

	7	8	9
$\tilde{C}$	-5.9814e-02	-1.2289e-01	-6.3080e-02
$\tilde{C}\left(\tau_{\text{SUPG}}\right)_{\text{UGN}}$	-2.9907e-02	-6.1446e-02	-3.1539e-02
$\tilde{C}\tau_{\text{SUPG}}$	-4.4859e-02	-9.2168e-02	-4.7308e-02
$\tilde{C}\left(\tau_{\text{SUPG}}\right)_{\text{V}}$	-7.7824e-01	-1.6252e+00	-8.4771e-01
	4	5	6
$\tilde{C}$	2.4533e-03	-9.8174e-02	-2.4533e-03
$\tilde{C}\left(\tau_{\text{SUPG}}\right)_{\text{UGN}}$	1.2266e-03	-4.9086e-02	-1.2266e-03
$\tilde{C}\tau_{\text{SUPG}}$	1.8399e-03	-7.3628e-02	-1.8399e-03
$\tilde{C}\left(\tau_{\text{SUPG}}\right)_{\text{V}}$	3.7560e-02	-6.7269e-01	-3.7722e-02
	1	2	3
$\tilde{C}$	1.3181e-02	2.4720e-02	1.1539e-02
$\tilde{C}\left(\tau_{\text{SUPG}}\right)_{\text{UGN}}$	6.5904e-03	1.2360e-02	5.7696e-03
$\tilde{C}\tau_{\text{SUPG}}$	9.8855e-03	1.8540e-02	8.6543e-03
$\tilde{C}\left(\tau_{\text{SUPG}}\right)_{\text{V}}$	5.0121e-01	9.5272e-01	4.5206e-01

Table 5.3: Assembled matrix ($\tilde{\mathbf{C}}$) and the product of $(\tau_{\text{SUPG}})_{\text{UGN}}$, τ_{SUPG}, and $(\tau_{\text{SUPG}})_{\text{V}}$ for triangular elements.

	7	8	9
$\tilde{K}$	3.6972e-05	-1.3593e-03	-3.6972e-05
$\tilde{K}\left(\tau_{\text{SUPG}}\right)_{\text{UGN}}$	1.8486e-05	-6.7962e-04	-1.8486e-05
$\tilde{K}\tau_{\text{SUPG}}$	2.7728e-05	-1.0194e-03	-2.7729e-05
$\tilde{K}\left(\tau_{\text{SUPG}}\right)_{\text{V}}$	4.7919e-04	-1.7966e-02	-4.9519e-04
	4	5	6
$\tilde{K}$	-1.1425e-05	1.4155e-03	1.0223e-05
$\tilde{K}\left(\tau_{\text{SUPG}}\right)_{\text{UGN}}$	-5.7125e-06	7.0772e-04	5.1116e-06
$\tilde{K}\tau_{\text{SUPG}}$	-8.5687e-06	1.0616e-03	7.6673e-06
$\tilde{K}\left(\tau_{\text{SUPG}}\right)_{\text{V}}$	-1.2168e-04	2.0113e-02	1.1295e-04
	1	2	3
$\tilde{K}$	-4.5651e-06	-5.4997e-05	4.5651e-06
$\tilde{K}\left(\tau_{\text{SUPG}}\right)_{\text{UGN}}$	-2.2825e-06	-2.7499e-05	2.2825e-06
$\tilde{K}\tau_{\text{SUPG}}$	-3.4238e-06	-4.1247e-05	3.4238e-06
$\tilde{K}\left(\tau_{\text{SUPG}}\right)_{\text{V}}$	-1.0931e-04	-2.1184e-03	1.0568e-04

Table 5.4: Assembled matrix ($\tilde{\mathbf{K}}$) and the product of $\left(\tau_{\text{SUPG}}\right)_{\text{UGN}}$, τ_{SUPG}, and $\left(\tau_{\text{SUPG}}\right)_{\text{V}}$ for triangular elements.

Generally, when multiplying the assembled matrices by EMB stabilization parameters, results closely match matrices multiplied by UGN stabilization parameters. When multiplying by EVB stabilization parameters, the matrix outcome is typically one to two orders of magnitude larger. The nature of the EVB stabilization parameters yields the considerably larger matrix values. Between quadrilateral and triangular element groupings, the trends reported in Section 5.1.2 still apply, with differences in magnitude present in both element types due to the altered velocity field.

5.2.2 Deformed Element Boundary Flow Assembly

This section compares the matrix assemblies presented previously to a case with vertical distortion for element groupings with an elemental aspect ratio of 100. A linear distortion is applied to the top of the element configuration, resulting in a 10% and 20% increase in the element height on the top-middle and top-right nodes, respectively. Figure 5.10 shows the distortion applied to the element groupings for quadrilaterals and triangles.

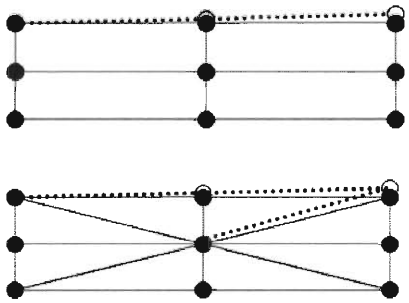

Figure 5.10: Element groupings with linear distortion along top edges for quadrilateral elements (top) and triangular elements (bottom). Dashed line represents the distorted connection between elements. Not shown to scale.

The assembled matrices, $\tilde{\mathbf{C}}$ and $\tilde{\mathbf{K}}$, are multiplied by each τ selection for the deformed element grouping. Tables 5.5 and 5.6 show deformed quadrilateral element groupings and Tables 5.7 and 5.8 show deformed triangular element groupings.

	7	8	9
$\tilde{C}$	-2.6669e-02	-1.1053e-01	-2.8686e-02
$\tilde{C}\,(\tau_{\text{SUPG}})_{\text{UGN}}$	-1.3335e-02	-5.5263e-02	-1.4343e-02
$\tilde{C}\tau_{\text{SUPG}}$	-1.3791e-02	-5.7250e-02	-1.4882e-02
$\tilde{C}\,(\tau_{\text{SUPG}})_{\text{V}}$	-3.5721e-01	-1.4817e+00	-3.8486e-01
	4	5	6
$\tilde{C}$	-1.5867e-02	-7.3630e-02	-2.1131e-02
$\tilde{C}\,(\tau_{\text{SUPG}})_{\text{UGN}}$	-7.9335e-03	-3.6815e-02	-1.0566e-02
$\tilde{C}\tau_{\text{SUPG}}$	-8.2105e-03	-3.8191e-02	-1.0982e-02
$\tilde{C}\,(\tau_{\text{SUPG}})_{\text{V}}$	-8.1466e-02	-4.9589e-01	-1.6896e-01
	1	2	3
$\tilde{C}$	9.5778e-03	3.7080e-02	8.9622e-03
$\tilde{C}\,(\tau_{\text{SUPG}})_{\text{UGN}}$	4.7889e-03	1.8540e-02	4.4811e-03
$\tilde{C}\tau_{\text{SUPG}}$	4.9479e-03	1.9156e-02	4.6299e-03
$\tilde{C}\,(\tau_{\text{SUPG}})_{\text{V}}$	2.5526e-01	9.8824e-01	2.3886e-01

Table 5.5: Assembled matrix ($\tilde{\mathbf{C}}$) and the product of $(\tau_{\text{SUPG}})_{\text{UGN}}$, τ_{SUPG}, and $(\tau_{\text{SUPG}})_{\text{V}}$ for quadrilateral deformed elements.

	7	8	9
$\tilde{K}$	-1.5663e-04	-6.6636e-04	-1.7791e-04
$\tilde{K}\,(\tau_{\text{SUPG}})_{\text{UGN}}$	-7.8312e-05	-3.3318e-04	-8.8955e-05
$\tilde{K}\tau_{\text{SUPG}}$	-8.0995e-05	-3.4513e-04	-9.2297e-05
$\tilde{K}\,(\tau_{\text{SUPG}})_{\text{V}}$	-2.0978e-03	-8.9324e-03	-2.3869e-03
	4	5	6
$\tilde{K}$	1.9481e-04	7.5028e-04	1.7956e-04
$\tilde{K}\,(\tau_{\text{SUPG}})_{\text{UGN}}$	9.7402e-05	3.7514e-04	8.9778e-05
$\tilde{K}\tau_{\text{SUPG}}$	1.0073e-04	3.8851e-04	9.3107e-05
$\tilde{K}\,(\tau_{\text{SUPG}})_{\text{V}}$	2.8820e-03	1.1152e-02	2.6814e-03
	1	2	3
$\tilde{K}$	-2.2701e-05	-8.2451e-05	-1.8592e-05
$\tilde{K}\,(\tau_{\text{SUPG}})_{\text{UGN}}$	-1.1350e-05	-4.1225e-05	-9.2962e-06
$\tilde{K}\tau_{\text{SUPG}}$	-1.1727e-05	-4.2594e-05	-9.6048e-06
$\tilde{K}\,(\tau_{\text{SUPG}})_{\text{V}}$	-6.0502e-04	-2.1974e-03	-4.9552e-04

Table 5.6: Assembled matrix ($\tilde{\mathbf{K}}$) and the product of $(\tau_{\text{SUPG}})_{\text{UGN}}$, τ_{SUPG}, and $(\tau_{\text{SUPG}})_{\text{V}}$ for quadrilateral deformed elements.

	7	8	9
$\tilde{C}$	-5.9611e-02	-1.2249e-01	-6.3203e-02
$\tilde{C}\left(\tau_{\text{SUPG}}\right)_{\text{UGN}}$	-2.9805e-02	-6.1243e-02	-3.1601e-02
$\tilde{C}\tau_{\text{SUPG}}$	-4.4707e-02	-9.1863e-02	-4.7401e-02
$\tilde{C}\left(\tau_{\text{SUPG}}\right)_{\text{V}}$	-7.7478e-01	-1.6209e+00	-8.5124e-01
	4	5	6
$\tilde{C}$	2.4533e-03	-9.8094e-02	-2.7798e-03
$\tilde{C}\left(\tau_{\text{SUPG}}\right)_{\text{UGN}}$	1.2266e-03	-4.9046e-02	-1.3899e-03
$\tilde{C}\tau_{\text{SUPG}}$	1.8399e-03	-7.3568e-02	-2.0848e-03
$\tilde{C}\left(\tau_{\text{SUPG}}\right)_{\text{V}}$	3.7560e-02	-6.7276e-01	-4.2150e-02
	1	2	3
$\tilde{C}$	1.3181e-02	2.4720e-02	1.1539e-02
$\tilde{C}\left(\tau_{\text{SUPG}}\right)_{\text{UGN}}$	6.5904e-03	1.2360e-02	5.7696e-03
$\tilde{C}\tau_{\text{SUPG}}$	9.8855e-03	1.8540e-02	8.6543e-03
$\tilde{C}\left(\tau_{\text{SUPG}}\right)_{\text{V}}$	5.0121e-01	9.5272e-01	4.5206e-01

Table 5.7: Assembled matrix ($\tilde{\mathbf{C}}$) and the product of $(\tau_{\text{SUPG}})_{\text{UGN}}$, τ_{SUPG}, and $(\tau_{\text{SUPG}})_{\text{V}}$ for triangular deformed elements.

	7	8	9
$\tilde{K}$	3.6898e-05	-1.2275e-03	-3.6898e-05
$\tilde{K}\left(\tau_{\text{SUPG}}\right)_{\text{UGN}}$	1.8449e-05	-6.1376e-04	-1.8449e-05
$\tilde{K}\tau_{\text{SUPG}}$	2.7673e-05	-9.2063e-04	-2.7673e-05
$\tilde{K}\left(\tau_{\text{SUPG}}\right)_{\text{V}}$	4.7792e-04	-1.6233e-02	-4.9545e-04
	4	5	6
$\tilde{K}$	-1.1425e-05	1.2838e-03	1.0127e-05
$\tilde{K}\left(\tau_{\text{SUPG}}\right)_{\text{UGN}}$	-5.7125e-06	6.4191e-04	5.0636e-06
$\tilde{K}\tau_{\text{SUPG}}$	-8.5687e-06	9.6285e-04	7.5954e-06
$\tilde{K}\left(\tau_{\text{SUPG}}\right)_{\text{V}}$	-1.2168e-04	1.8382e-02	1.1224e-04
	1	2	3
$\tilde{K}$	-4.5651e-06	-5.4997e-05	4.5651e-06
$\tilde{K}\left(\tau_{\text{SUPG}}\right)_{\text{UGN}}$	-2.2825e-06	-2.7499e-05	2.2825e-06
$\tilde{K}\tau_{\text{SUPG}}$	-3.4238e-06	-4.1247e-05	3.4238e-06
$\tilde{K}\left(\tau_{\text{SUPG}}\right)_{\text{V}}$	-1.0931e-04	-2.1184e-03	1.0568e-04

Table 5.8: Assembled matrix ($\tilde{\mathbf{K}}$) and the product of $(\tau_{\text{SUPG}})_{\text{UGN}}$, τ_{SUPG}, and $(\tau_{\text{SUPG}})_{\text{V}}$ for triangular deformed elements.

The impact of deformation on element grouping is more easily identifiable using the percent difference of matrix outcomes between the undeformed and deformed shapes. No differences between assembled matrices were identified in the bottom three nodes; therefore, those values are not included in the tables. Tables 5.9 and 5.10 show the percent difference of matrix outcomes for quadrilateral element groupings and Tables 5.11 and 5.12 show the percent difference for triangular element groupings.

	7	8	9
$\tilde{C}$	-0.34	-0.17	0.32
$\tilde{C}\left(\tau_{\text{SUPG}}\right)_{\text{UGN}}$	-0.34	-0.17	0.32
$\tilde{C}\tau_{\text{SUPG}}$	-0.23	0.11	0.75
$\tilde{C}\left(\tau_{\text{SUPG}}\right)_{\text{V}}$	-0.34	-0.17	0.32
	4	5	6
$\tilde{C}$	-0.57	0.00	1.32
$\tilde{C}\left(\tau_{\text{SUPG}}\right)_{\text{UGN}}$	-0.57	0.00	1.32
$\tilde{C}\tau_{\text{SUPG}}$	-0.40	0.42	1.93
$\tilde{C}\left(\tau_{\text{SUPG}}\right)_{\text{V}}$	-1.54	0.00	2.27

Table 5.9: Percent difference comparison of the undeformed and deformed quadrilateral element groupings for the product of $(\tau_{\text{SUPG}})_{\text{UGN}}$, τ_{SUPG}, and $(\tau_{\text{SUPG}})_{\text{V}}$ and assembled matrix ($\tilde{\mathbf{C}}$).

	7	8	9
$\tilde{K}$	-5.53	-9.34	-12.07
$\tilde{K}\left(\tau_{\text{SUPG}}\right)_{\text{UGN}}$	-5.55	-9.33	-12.06
$\tilde{K}\tau_{\text{SUPG}}$	-5.37	-9.11	-11.67
$\tilde{K}\left(\tau_{\text{SUPG}}\right)_{\text{V}}$	-5.53	-9.34	-12.06
	4	5	6
$\tilde{K}$	-4.52	-8.37	-11.99
$\tilde{K}\left(\tau_{\text{SUPG}}\right)_{\text{UGN}}$	-4.51	-8.38	-11.96
$\tilde{K}\tau_{\text{SUPG}}$	-4.46	-8.16	-11.67
$\tilde{K}\left(\tau_{\text{SUPG}}\right)_{\text{V}}$	-4.10	-7.59	-10.88

Table 5.10: Percent difference comparison of the undeformed and deformed quadrilateral element groupings for the product of $(\tau_{\text{SUPG}})_{\text{UGN}}$, τ_{SUPG}, and $(\tau_{\text{SUPG}})_{\text{V}}$ and assembled matrix ($\tilde{\mathbf{K}}$).

	7	8	9
$\tilde{C}$	-0.34	-0.33	0.20
$\tilde{C}\,(\tau_{\text{SUPG}})_{\text{UGN}}$	-0.34	-0.33	0.19
$\tilde{C}\tau_{\text{SUPG}}$	-0.34	-0.33	0.20
$\tilde{C}\,(\tau_{\text{SUPG}})_{\text{V}}$	-0.68	-0.49	0.19
	4	5	6
$\tilde{C}$	0.00	-0.08	13.31
$\tilde{C}\,(\tau_{\text{SUPG}})_{\text{UGN}}$	0.00	-0.08	13.31
$\tilde{C}\tau_{\text{SUPG}}$	0.00	-0.08	13.30
$\tilde{C}\,(\tau_{\text{SUPG}})_{\text{V}}$	0.00	-0.57	11.51

Table 5.11: Percent difference comparison of the undeformed and deformed triangular element groupings for the product of $(\tau_{\text{SUPG}})_{\text{UGN}}$, τ_{SUPG}, and $(\tau_{\text{SUPG}})_{\text{V}}$ and assembled matrix ($\tilde{\mathbf{C}}$).

	7	8	9
$\tilde{K}$	-0.19	-9.69	-0.19
$\tilde{K}\,(\tau_{\text{SUPG}})_{\text{UGN}}$	-0.54	-9.68	-0.54
$\tilde{K}\tau_{\text{SUPG}}$	0.00	-9.69	0.00
$\tilde{K}\,(\tau_{\text{SUPG}})_{\text{V}}$	-0.39	-9.85	-0.20
	4	5	6
$\tilde{K}$	0.00	-9.30	-0.88
$\tilde{K}\,(\tau_{\text{SUPG}})_{\text{UGN}}$	0.00	-9.30	0.00
$\tilde{K}\tau_{\text{SUPG}}$	0.00	-9.30	-1.30
$\tilde{K}\,(\tau_{\text{SUPG}})_{\text{V}}$	0.00	-8.76	-1.06

Table 5.12: Percent difference comparison of the undeformed and deformed quadrilateral element groupings for the product of $(\tau_{\text{SUPG}})_{\text{UGN}}$, τ_{SUPG}, and $(\tau_{\text{SUPG}})_{\text{V}}$ and assembled matrix ($\tilde{\mathbf{K}}$).

The use of high aspect ratio quadrilateral elements is sometimes preferred over triangular elements in the boundary layer due to the generation of "bad elements" more common in high aspect ratio triangles. However, distortion to elements near the boundary layer is typically minimized to avoid bad elements for both shapes. It is important to understand that significant impact to the stabilization terms does not necessarily dictate the overall accuracy of the solution.

The percent difference comparison emphasizes several differences in stabilization terms for different element type and τ selection. In a comparison of the change in matrix assembly due to a small distortion for all τ types, the change in the product is the same order of magnitude as the change in the matrix multiplied by τ. Through the percent difference analysis, additional comparisons between quadrilateral and triangular elements were noted. Aside from specific trends noted below, most matrix assembly results were comparable. Inspection of the $\tilde{\mathbf{C}}$ matrix assembly showed approximately 13% difference in triangular element configurations at node six compared to a 2% at the same node for quadrilaterals. The $\tilde{\mathbf{K}}$ matrix assembly yielded more significant differences in more nodes, with nodes six and nine showing between 10 to 12% difference and 0 to 2% difference for quadrilaterals and triangles, respectively. Nodes four and seven also yielded results that varied up to 5% between element types. Generally, triangular groupings exhibited more significant changes in the $\tilde{\mathbf{C}}$ matrix calculations at the top-right node where distortion was highest, whereas quadrilaterals exhibited more significant changes in $\tilde{\mathbf{K}}$ matrix calculations on side nodes.

Chapter 6

Test Computations

This chapter presents semi-discrete computations of incompressible flow past a circular cylinder and provides a comparison of the currently-used and alternative stabilization parameters, both EMB and EVB. Flow computations are performed at a Reynolds number of 100 to compare to previous results reported in [30, 24]. In addition to a quadrilateral mesh, a triangular mesh is used in order to investigate stabilization parameter implications based on element type.

6.1 2D Cylinder Mesh

A 2D computation of incompressible flow past a circular cylinder is used for testing of all stabilization parameters here. A cylinder with a radius, R, of one unit is located at the origin of the computational domain. The upstream, downstream, and cross flow boundaries of the domain are located 16, 45, and 16 units from the origin. The mesh consists of 4,558 nodes and 4,424 quadrilateral elements or 8,848 triangular elements. There are 64 elements in the circumferential direction. This thesis focuses on boundary layer elements; therefore, the first four layers of elements around the cylinder have an aspect ratio of 100 and a constant element height. The triangular elements are generated by a diagonal split of each quadrilateral element,

with symmetry along the horizontal axis. Figures 6.1 and 6.2 depict the quadrilateral mesh used for computations and Figures 6.3 and 6.4 depict the triangular mesh used for computations.

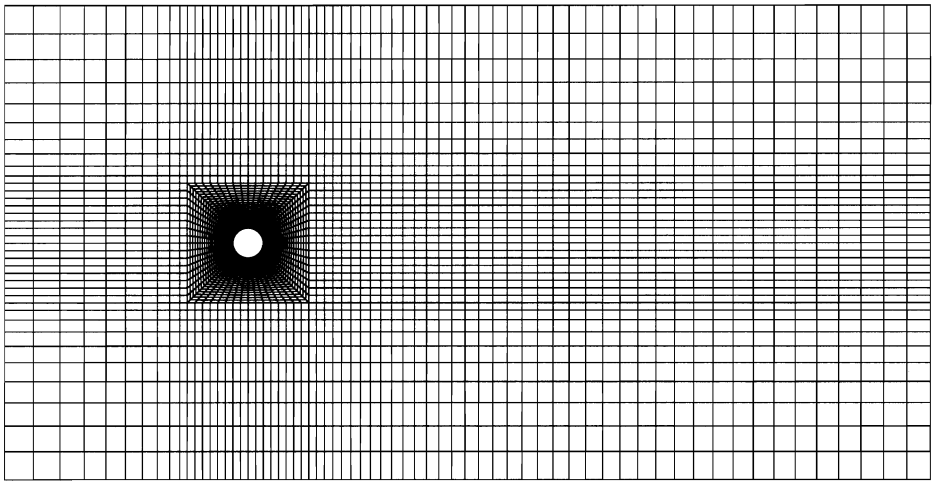

Figure 6.1: Quadrilateral mesh.

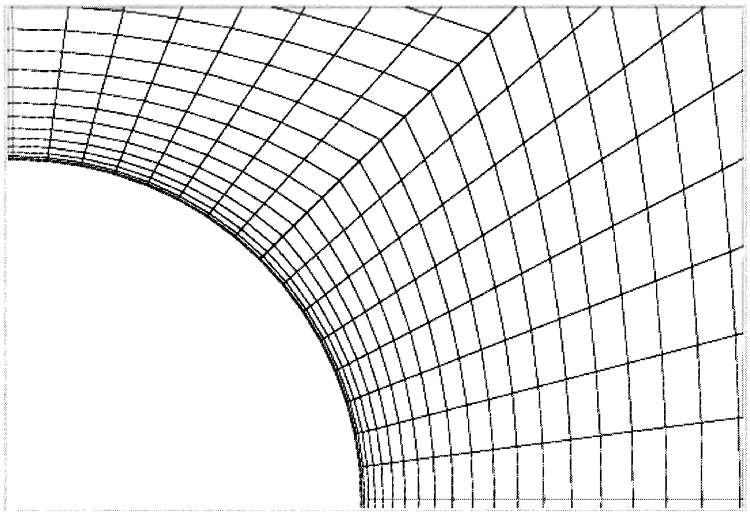

Figure 6.2: Quadrilateral mesh zoomed view near boundary.

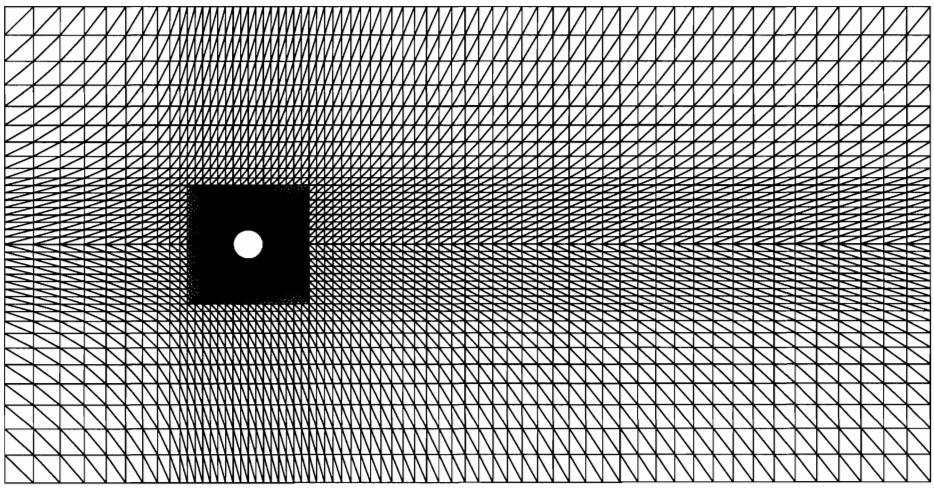

Figure 6.3: Triangular mesh.

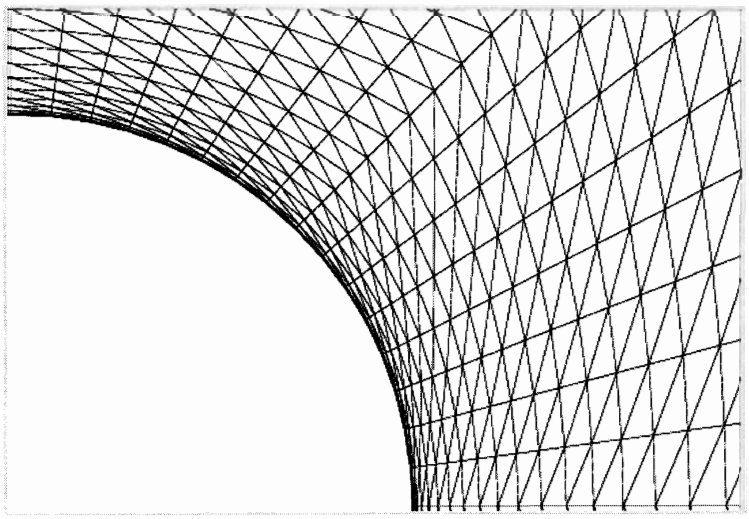

Figure 6.4: Triangular mesh zoomed view near boundary.

For all computations, $U_\infty = 1$, where U_∞ is the free-stream velocity. The boundary conditions consist of uniform inflow velocity, slip condition at the lateral boundaries, traction-free condition at the outflow boundary, and no-slip condition on the cylinder.

6.2 2D Incompressible Flow Past a Cylinder with Vortex Shedding

The flow should exhibit vortex shedding at Re=100. The time step, $\triangle t$, is 0.1. Three Newton–Raphson iterations are performed at every time step. At each Newton–Raphson step, the linear equation system encountered is solved iteratively with 90 GMRES iterations [21]. The UGN stabilization parameters are used for the computation until a temporally-periodic solution is reached. At that point, the UGN, EMB, and EVB stabilization parameters are calculated using the computed flow field.

The stabilization parameters show similar trends to those documented in [30]. As described in Chapter 3, the currently-used stabilization parameters assign $(\tau_{\text{SUPG}})_{\text{UGN}} = (\tau_{\text{PSPG}})_{\text{UGN}}$. The plots and figures are shown for zero lift during the period of vortex shedding. Figures 6.5 and 6.6 show the stabilization parameters along the vertical axis beginning at the top of the cylinder for the quadrilateral mesh. Figures 6.13 and 6.14 show the stabilization parameters along the same axis for a triangular mesh.

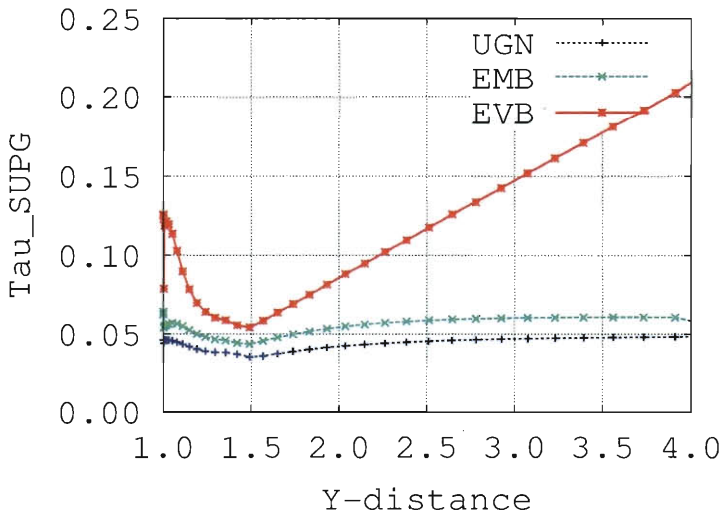

Figure 6.5: Plot of SUPG stabilization parameters along vertical axis from cylinder center for quadrilateral mesh.

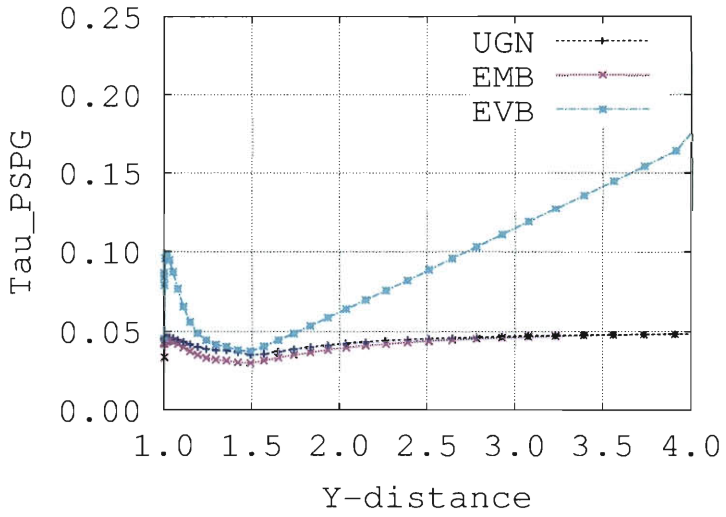

Figure 6.6: Plot of PSPG stabilization parameters along vertical axis from cylinder center for quadrilateral mesh.

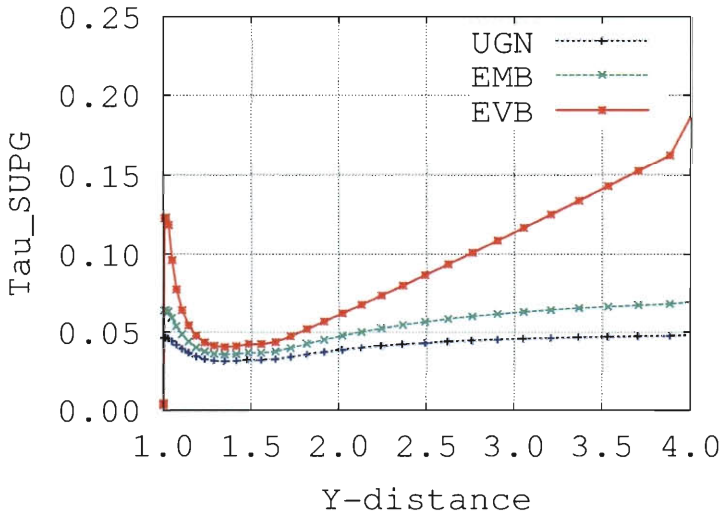

Figure 6.7: Plot of SUPG stabilization parameters along vertical axis from cylinder center for triangular mesh.

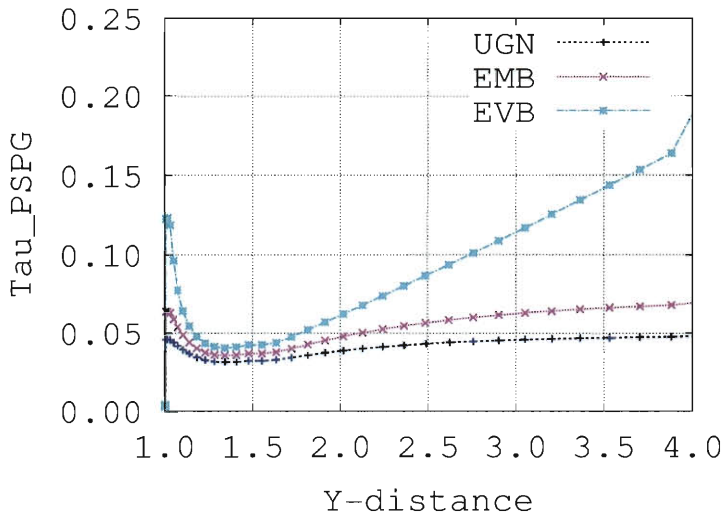

Figure 6.8: Plot of PSPG stabilization parameters along vertical axis from cylinder center for triangular mesh.

The flow characteristics from this case match previous results, with a Strouhal number of 0.167. For all cases with the original mesh shown in Figure 6.1, the area very close to the boundary layer shows a significant dip for EVB stabilization parameters. This dip is likely attributed to the thin boundary layer elements next to the cylinder. Additionally, the flow characteristics exhibit some oscillations with this mesh. We also tested an alternative mesh that combines the first four layers of the original mesh into one layer. This means that the largest aspect ratio for the boundary layer elements is 25. The modified mesh consists of 4,366 nodes and 4,232 elements or 8,464 elements for the quadrilateral mesh and triangular mesh, respectively. Figures 6.9 and 6.10 provide a view of the original and modified boundary layer meshes for quadrilateral and triangular cases, respectively.

Table 6.1 shows the Strouhal number and the average drag coefficient for the quadrilateral and triangular meshes.

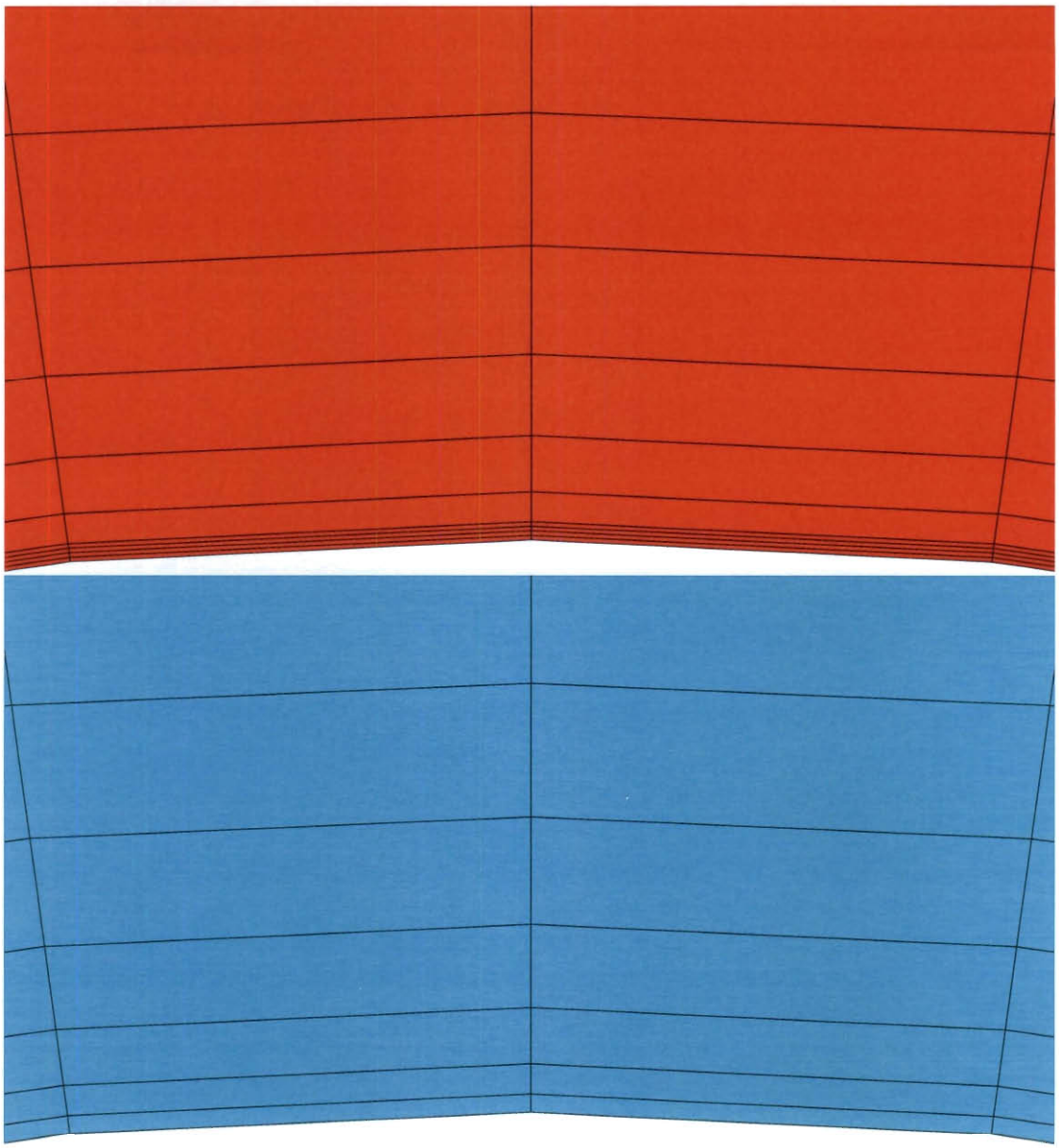

Figure 6.9: Boundary layer mesh refinement for quadrilateral mesh. Original mesh (top). Modified mesh (bottom).

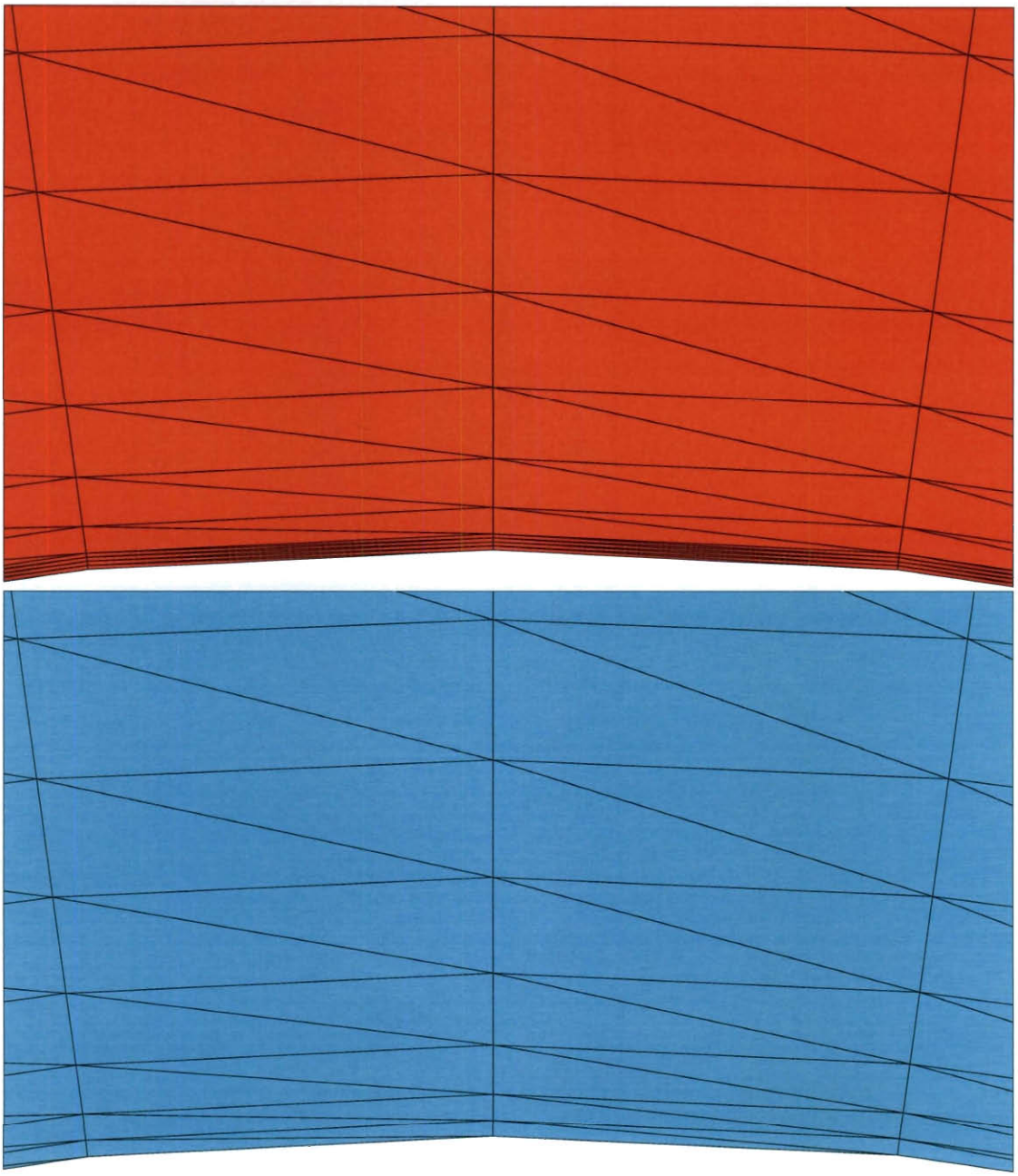

Figure 6.10: Boundary layer mesh refinement for triangular mesh. Original mesh (top). Modified mesh (bottom).

Figures 6.11 and 6.12 show the value of SUPG and PSPG stabilization parameters along the vertical axis from the cylinder center for the modified quadrilateral mesh and Figures 6.13 and 6.14 show the value of SUPG and PSPG stabilization parameters for the modified triangular mesh. These plots show that the dip for EVB τ is eliminated with the thicker boundary layer mesh. Additionally, the numerical oscillations in the drag history are eliminated. The high aspect-ratio elements do not yield very accurate results for low Reynolds number flow, exhibited by the flow characteristics and stabilization parameters. Table 6.1 shows the Strouhal number and the average drag coefficient for the original and modified meshes for both element types.

	Strouhal Number	Average Drag Coefficient
Original Quadrilateral Mesh (4 layer)	0.167	1.391
Modified Quadrilateral Mesh (1 layer)	0.169	1.410
Original Triangular Mesh (4 layer)	0.161	1.379
Modified Triangular Mesh (1 layer)	0.167	1.399

Table 6.1: Flow characteristics comparison for different mesh types.

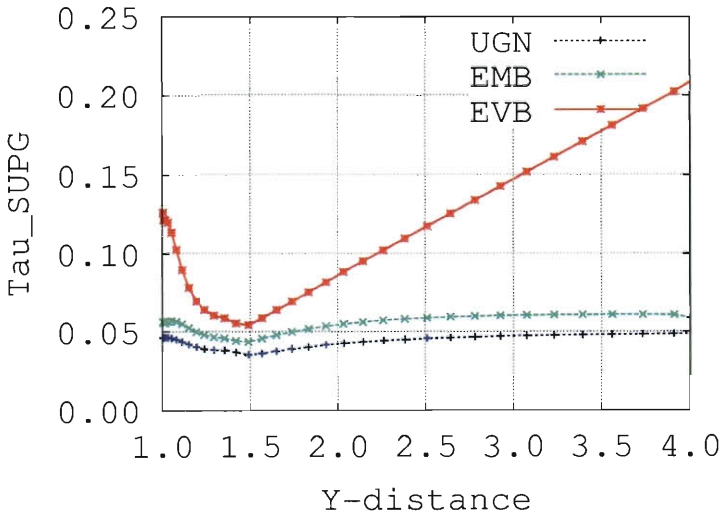

Figure 6.11: Plot of SUPG stabilization parameters along vertical axis from cylinder center for modified quadrilateral mesh.

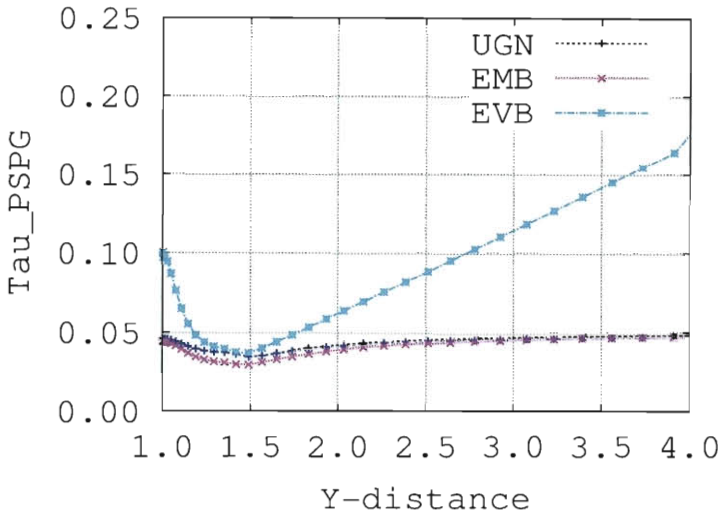

Figure 6.12: Plot of PSPG stabilization parameters along vertical axis from cylinder center for modified quadrilateral mesh.

Figures 6.15 and 6.16 show the time history of lift and drag coefficients for the modified quadrilateral mesh and Figures 6.17 and 6.18 show the time history of lift and drag coefficients for the modified triangular mesh. Figures 6.19 and 6.20 visualize the spatial distribution of the stabilization parameters for the modified quadrilateral mesh and Figures 6.21 and 6.22 visualize the spatial distribution of the stabilization parameters for the modified triangular mesh.

The visualization shows that the currently-used and EMB stabilization parameters correlate well. Similar values are exhibited in most regions of the mesh, with the EMB values slightly larger but within the same order of magnitude. The EVB results show much larger values of τ, ranging up to two orders of magnitude in difference to the other τ definitions. This trend correlates with the trends shown in the τ plots.

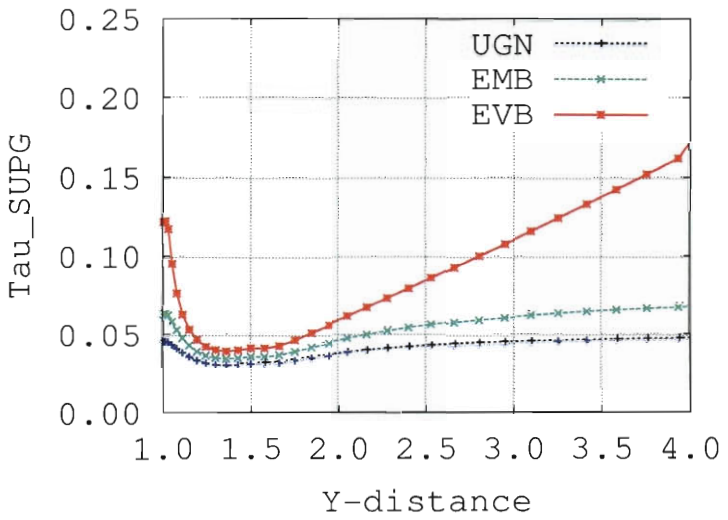

Figure 6.13: Plot of SUPG stabilization parameters along vertical axis from cylinder center for modified triangular mesh.

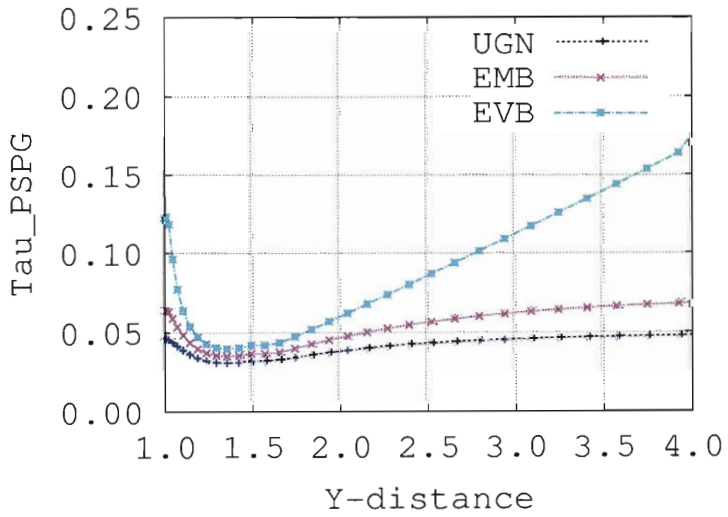

Figure 6.14: Plot of PSPG stabilization parameters along vertical axis from cylinder center for modified triangular mesh.

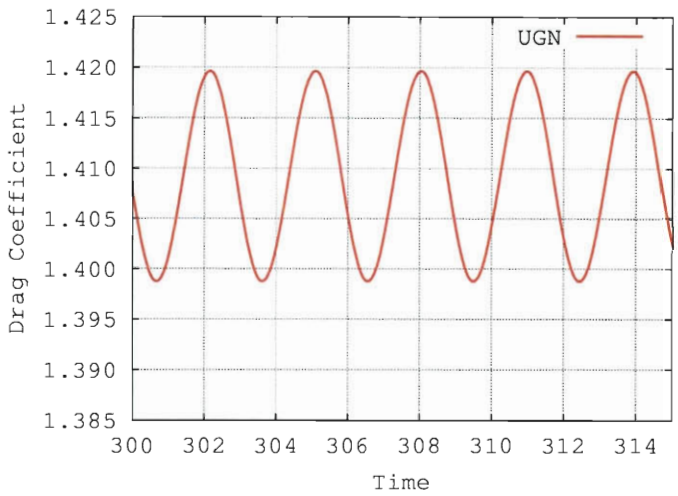

Figure 6.15: Time history of the drag coefficient for the modified quadrilateral mesh.

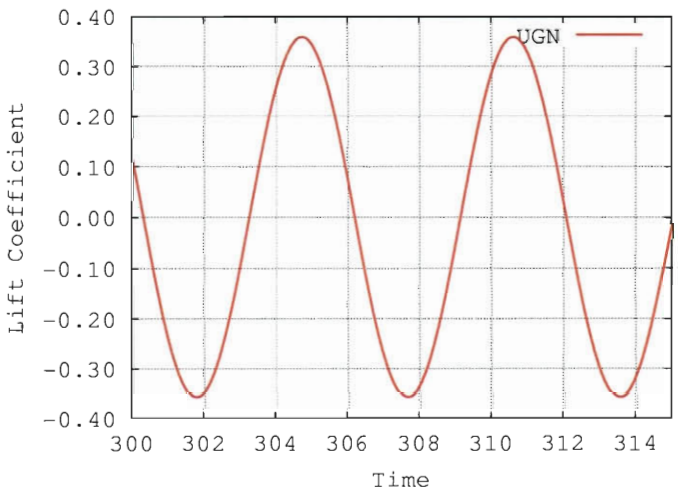

Figure 6.16: Time history of the lift coefficient for the modified quadrilateral mesh.

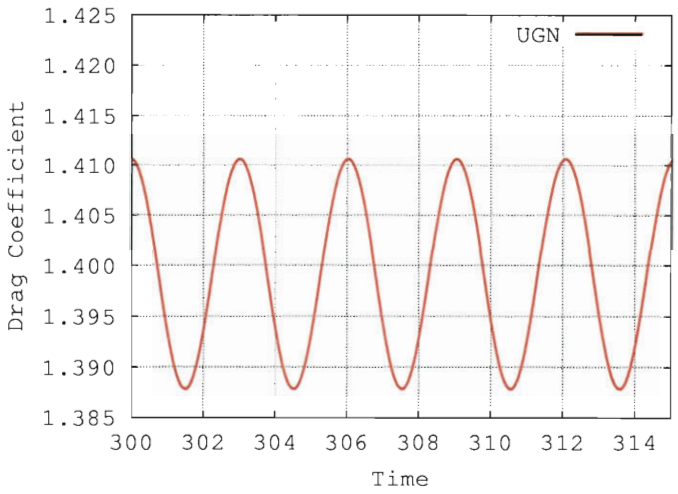

Figure 6.17: Time history of the drag coefficient for the modified triangular mesh.

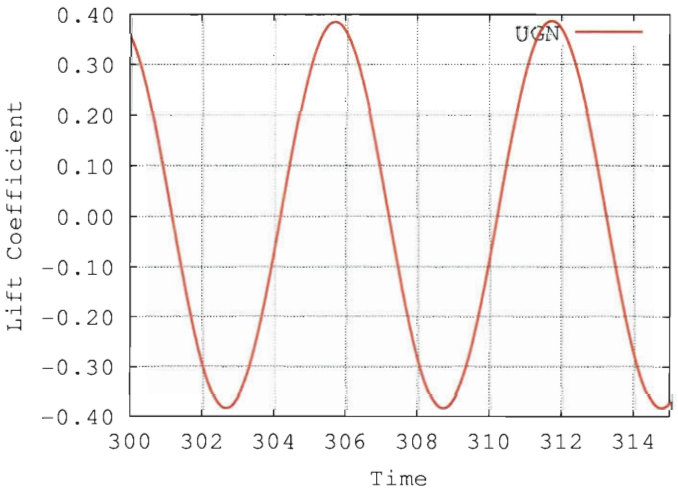

Figure 6.18: Time history of the lift coefficient for the modified triangular mesh.

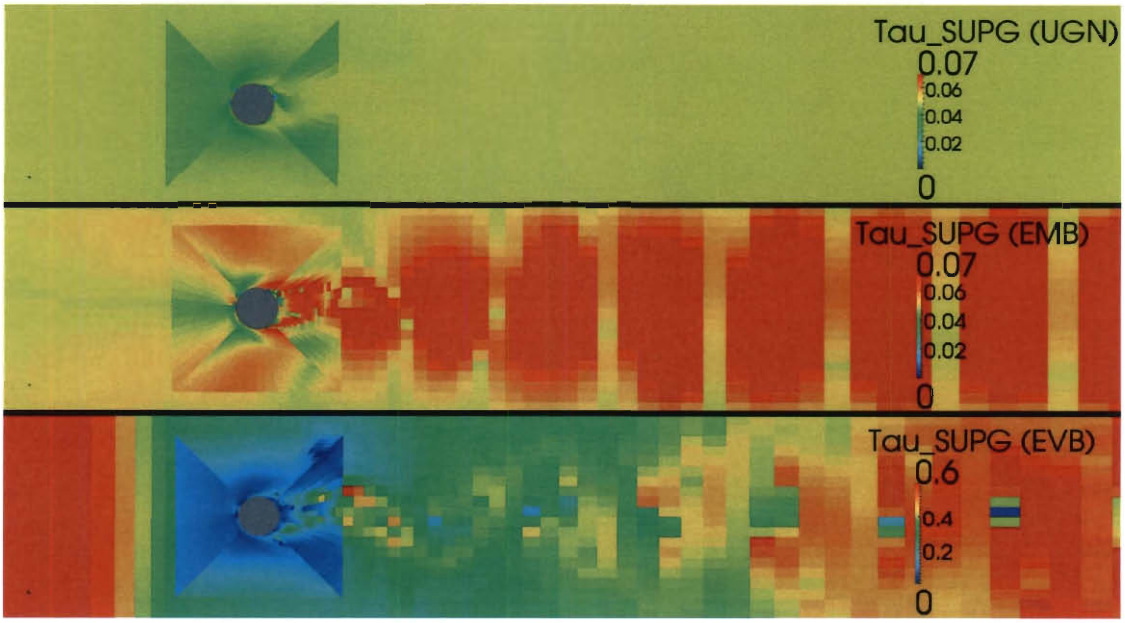

Figure 6.19: Visualization of the SUPG stabilization parameters for modified quadrilateral mesh.

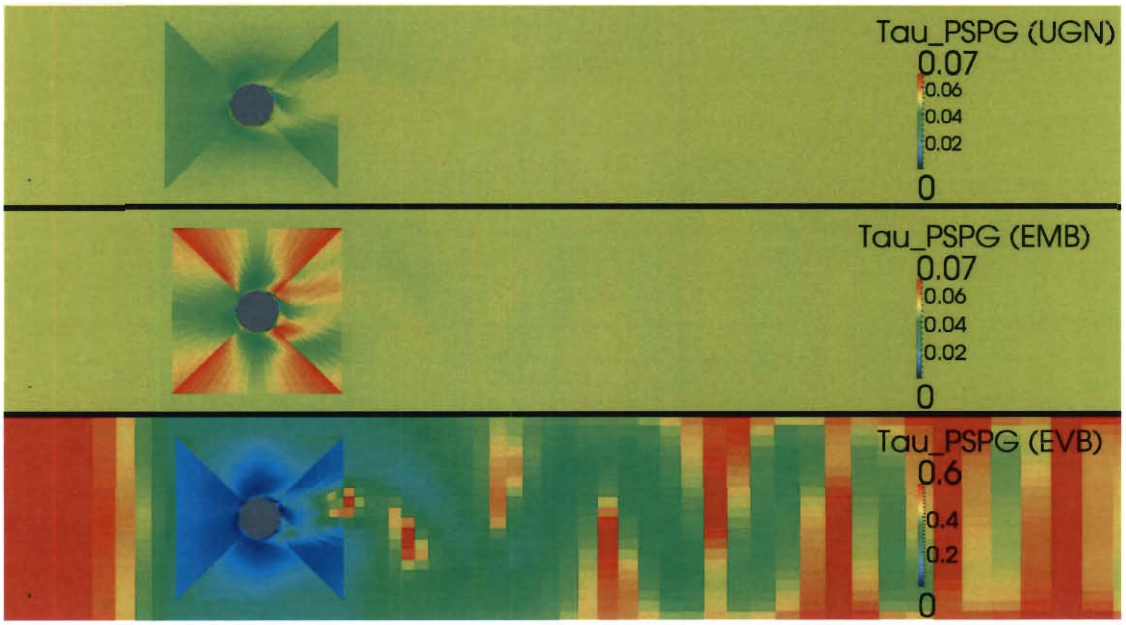

Figure 6.20: Visualization of the PSPG stabilization parameters for modified quadrilateral mesh.

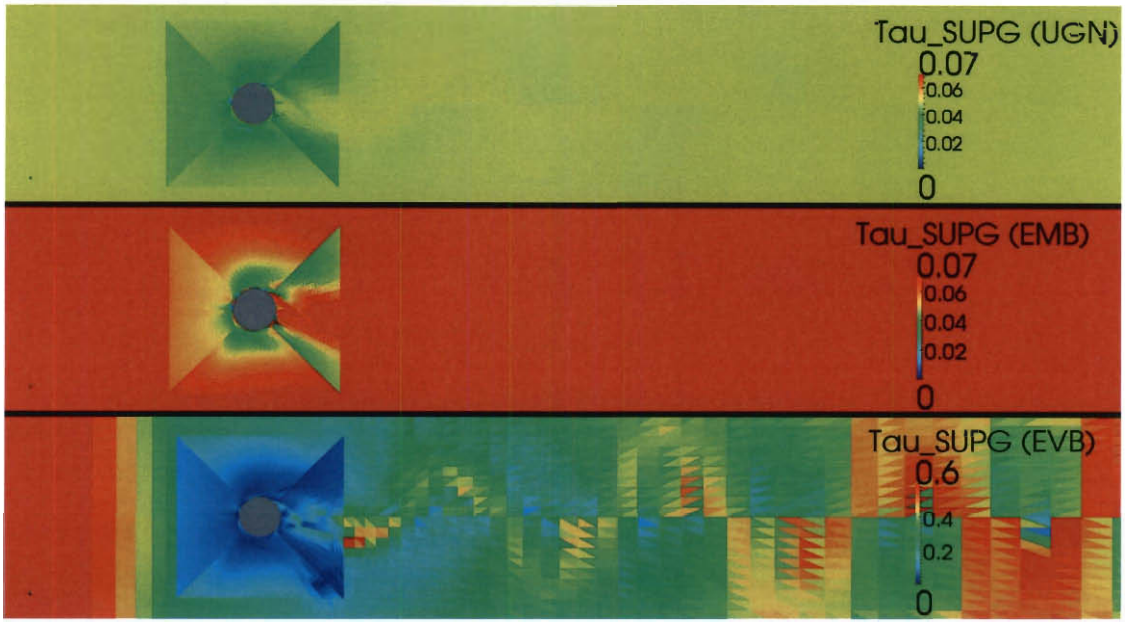

Figure 6.21: Visualization of the SUPG stabilization parameters for modified quadrilateral mesh.

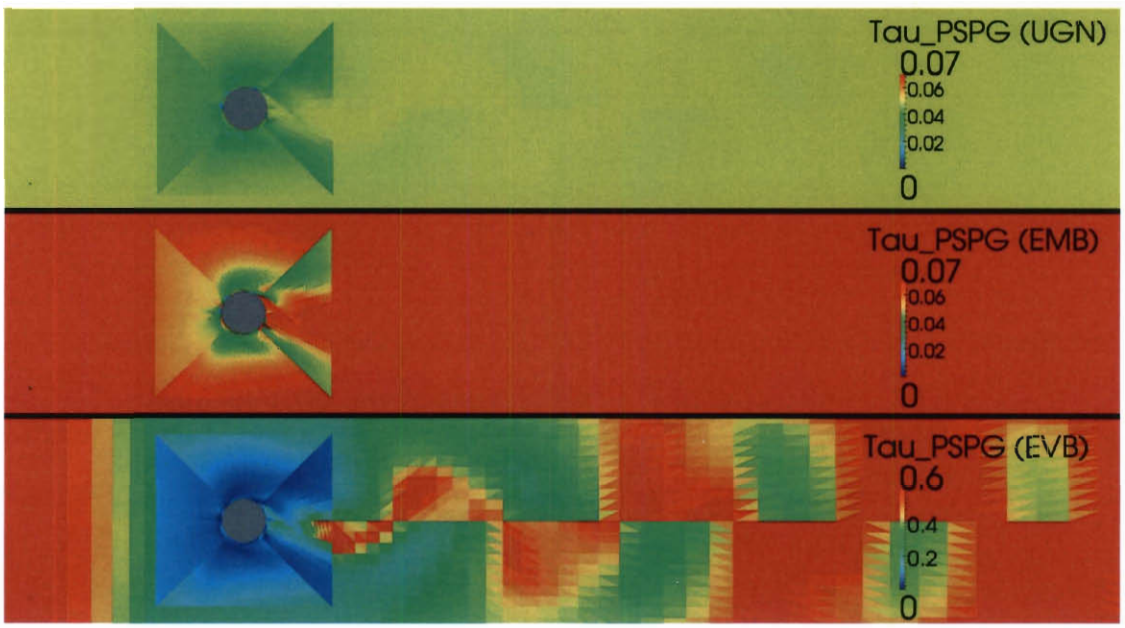

Figure 6.22: Visualization of the PSPG stabilization parameters for modified quadrilateral mesh.

Chapter 7

Conclusions

Stabilization parameters play a significant role in stabilized formulations. This thesis provides an overview of currently-used and alternative stabilization parameters calculated from element-level matrices and vectors for SUPG and PSPG stabilizations. The currently-used stabilization parameters provide a basis for comparison to the alternative stabilization techniques presented in [30, 24] for flow problems governed by the advection–diffusion and Navier–Stokes equations. Detailed representations of stabilization parameters are presented for different element shapes, for the effect of τ on stabilization terms, and in computations, to show the trends associated with various stabilization techniques, placing particular attention on boundary layer elements and the type of element. The alternative stabilization parameters can, in some cases, produce τ values and stabilization terms similar to those currently used.

Bibliography

[1] J. E. Akin, T. Tezduyar, M. Ungor, and S. Mittal. Stabilization parameters and Smagorinsky turbulence model. *Journal of Applied Mechanics*, 70:2–9, 2003.

[2] J. E. Akin and T. E. Tezduyar. Calculation of the advective limit of the SUPG stabilization parameter for linear and higher-order elements. *Computer Methods in Applied Mechanics and Engineering*, 193:1909–1922, 2004.

[3] Y. Bazilevs and I. Akkerman. Large eddy simulation of turbulent Taylor–Couette flow using isogeometric analysis and the residual–based variational multiscale method. *Journal of Computational Physics*, 229:3402–3414, 2010.

[4] Y. Bazilevs, V. M. Calo, J. A. Cottrel, T. J. R. Hughes, A. Reali, and G. Scovazzi. Variational multiscale residual-based turbulence modeling for large eddy simulation of incompressible flows. *Computer Methods in Applied Mechanics and Engineering*, 197:173–201, 2007.

[5] A. N. Brooks and T. J. R. Hughes. Streamline upwind/Petrov-Galerkin formulations for convection dominated flows with particular emphasis on the incompressible Navier-Stokes equations. 32:199–259, 1982.

[6] L. Catabriga, A. L. G. A. Coutinho, and T. E. Tezduyar. Compressible flow SUPG stabilization parameters computed from element-edge matrices. *Computational Fluid Dynamics Journal*, 13:450–459, 2004.

[7] L. Catabriga, A. L. G. A. Coutinho, and T. E. Tezduyar. Compressible flow SUPG parameters computed from element matrices. *Communications in Numerical Methods in Engineering*, 21:465–476, 2005.

[8] L. Catabriga, A. L. G. A. Coutinho, and T. E. Tezduyar. Compressible flow SUPG parameters computed from degree-of-freedom submatrices. *Computational Mechanics*, 38:334–343, 2006.

[9] A. Corsini, F. Rispoli, A. Santoriello, and T. E. Tezduyar. Improved discontinuity-capturing finite element techniques for reaction effects in turbulence computation. *Computational Mechanics*, 38:356–364, 2006.

[10] L. P. Franca, S. L. Frey, and T. J. R. Hughes. Stabilized finite element methods: I. Application to the advective-diffusive model. *Computer Methods in Applied Mechanics and Engineering*, 95:253–276, 1992.

[11] M.-C. Hsu, Y. Bazilevs, V. M. Calo, T. E. Tezduyar, and T. J. R. Hughes. Improving stability of stabilized and multiscale formulations in flow simulations at small time steps. *Computer Methods in Applied Mechanics and Engineering*, 199:828–840, 2010.

[12] T. J. R. Hughes. Multiscale phenomena: Green's functions, the Dirichlet-to-Neumann formulation, subgrid scale models, bubbles, and the origins of stabilized methods. *Computer Methods in Applied Mechanics and Engineering*, 127:387–401, 1995.

[13] T. J. R. Hughes and A. N. Brooks. A multi-dimensional upwind scheme with no crosswind diffusion. In T. J. R. Hughes, editor, *Finite Element Methods for Convection Dominated Flows*, AMD-Vol.34, pages 19–35. ASME, New York, 1979.

[14] T. J. R. Hughes, L. P. Franca, and M. Balestra. A new finite element formulation for computational fluid dynamics: V. Circumventing the Babuška–Brezzi condition: A stable Petrov–Galerkin formulation of the Stokes problem accommodating equal-order interpolations. *Computer Methods in Applied Mechanics and Engineering*, 59:85–99, 1986.

[15] T. J. R. Hughes, M. Mallet, and A. Mizukami. A new finite element formulation for computational fluid dynamics: II. Beyond SUPG. *Computer Methods in Applied Mechanics and Engineering*, 54:341–355, 1986.

[16] T. J. R. Hughes, L. Mazzei, and K. E. Jansen. Large-eddy simulation and the variational multiscale method. *Computing and Visualization in Science*, 3:47–59, 2000.

[17] T. J. R. Hughes, A. A. Oberai, and L. Mazzei. Large eddy simulation of turbulent channel flows by the variational multiscale method. *Physics of Fluids*, 13:1784–1799, 2001.

[18] T. J. R. Hughes and G. Sangalli. Variational multiscale analysis: the fine-scale Green's function, projection, optimization, localization, and stabilized methods. *SIAM Journal of Numerical Analysis*, 45:539–557, 2007.

[19] T. J. R. Hughes and T. E. Tezduyar. Finite element methods for first-order hyperbolic systems with particular emphasis on the compressible Euler equations. *Computer Methods in Applied Mechanics and Engineering*, 45:217–284, 1984.

[20] F. Rispoli, A. Corsini, and T. E. Tezduyar. Finite element computation of turbulent flows with the discontinuity-capturing directional dissipation (DCDD). *Computers & Fluids*, 36:121–126, 2007.

[21] Y. Saad and M. Schultz. GMRES: A generalized minimal residual algorithm for solving nonsymmetric linear systems. *SIAM Journal of Scientific and Statistical Computing*, 7:856–869, 1986.

[22] T. E. Tezduyar. Stabilized finite element formulations for incompressible flow computations. *Advances in Applied Mechanics*, 28:1–44, 1992.

[23] T. E. Tezduyar. Adaptive determination of the finite element stabilization parameters. In *Proceedings of the ECCOMAS Computational Fluid Dynamics Conference 2001 (CD-ROM)*, Swansea, Wales, United Kingdom, 2001.

[24] T. E. Tezduyar. Computation of moving boundaries and interfaces and stabilization parameters. *International Journal for Numerical Methods in Fluids*, 43:555–575, 2003.

[25] T. E. Tezduyar. Finite element methods for fluid dynamics with moving boundaries and interfaces. In E. Stein, R. D. Borst, and T. J. R. Hughes, editors, *Encyclopedia of Computational Mechanics*, Volume 3: Fluids, chapter 17. John Wiley & Sons, 2004.

[26] T. E. Tezduyar, M. Behr, and J. Liou. A new strategy for finite element computations involving moving boundaries and interfaces – the deforming-spatial-domain/space–time procedure: I. The concept and the preliminary numerical tests. *Computer Methods in Applied Mechanics and Engineering*, 94(3):339–351, 1992.

[27] T. E. Tezduyar, M. Behr, S. Mittal, and J. Liou. A new strategy for finite element computations involving moving boundaries and interfaces – the deforming-spatial-domain/space–time procedure: II. Computation of free-surface flows, two-liquid flows, and flows with drifting cylinders. *Computer Methods in Applied Mechanics and Engineering*, 94(3):353–371, 1992.

[28] T. E. Tezduyar and T. J. R. Hughes. Finite element formulations for convection dominated flows with particular emphasis on the compressible Euler equations. In *Proceedings of AIAA 21st Aerospace Sciences Meeting*, AIAA Paper 83-0125, Reno, Nevada, 1983.

[29] T. E. Tezduyar, S. Mittal, S. E. Ray, and R. Shih. Incompressible flow computations with stabilized bilinear and linear equal-order-interpolation velocity-pressure elements. *Computer Methods in Applied Mechanics and Engineering*, 95:221–242, 1992.

[30] T. E. Tezduyar and Y. Osawa. Finite element stabilization parameters computed from element matrices and vectors. *Computer Methods in Applied Mechanics and Engineering*, 190:411–430, 2000.

[31] T. E. Tezduyar and Y. J. Park. Discontinuity capturing finite element formulations for nonlinear convection-diffusion-reaction equations. *Computer Methods in Applied Mechanics and Engineering*, 59:307–325, 1986.

[32] T. E. Tezduyar, Y. J. Park, and H. A. Deans. Finite element procedures for time-dependent convection-diffusion-reaction systems. *International Journal for Numerical Methods in Fluids*, 7:1013–1033, 1987.

[33] T. E. Tezduyar, S. Ramakrishnan, and S. Sathe. Stabilized formulations for incompressible flows with thermal coupling. *International Journal for Numerical Methods in Fluids*, 57:1189–1209, 2008.

[34] T. E. Tezduyar and S. Sathe. Enhanced-discretization space-time technique (EDSTT). *Computer Methods in Applied Mechanics and Engineering*, 193:1385–1401, 2004.

[35] T. E. Tezduyar and S. Sathe. Modeling of fluid–structure interactions with the space–time finite elements: Solution techniques. *International Journal for Numerical Methods in Fluids*, 54:855–900, 2007.